Generation of Earth's Early Continents From a Relatively Cool Archean Mantle

A Preprint

Andrea Piccolo
Institute of Geosciences
Johannes Gutenberg University
Mainz, Germany.
`piccolo@uni-mainz.de`

Boris J.P. Kaus
Institute of Geosciences
Johannes Gutenberg University
Mainz, Germany.

Richard W. White
School of Earth and Environmental Sciences
University of St Andrews
St Andrews, UK

Richard M. Palin
Department of Geology and Geological Engineering
Colorado School of Mines, Golden
Colorado, USA

Friday 21st May, 2021

Abstract

Several lines of evidence suggest that the Archean (4.0–2.5 Ga) mantle was hotter than today's potential temperature (T_P) of 1350 °C. However, the magnitude of such difference is poorly constrained, with T_P estimation spanning from 1500 °C to 1600 °C during the Meso-Archean (3.2-2.8 Ga). Such differences have major implications for the interpreted mechanisms of continental crust generation on the early Earth, as their efficacy is highly sensitive to the T_P. Here, we integrate petrological modeling with thermo-mechanical simulations to understand the dynamics of crust formation during Archean. Our results predict that partial melting of primitive oceanic crust produces felsic melts with geochemical signatures matching those observed in Archean cratons from a mantle T_P as low as 1450 °C thanks to lithospheric-scale Rayleigh–Taylor-type instabilities. These simulations also infer the occurrence of intraplate deformation events that allow an efficient transport of crustal material into the mantle, hydrating it.

1 Introduction

The Earth's earliest-formed continental crust is characterized by tonalite, trondhjemite and granodiorite (TTG) (Jahn et al., 1981) that are widely accepted to have been produced via high-temperature partial melting of hydrous meta-basalts (Moyen and Martin, 2012). While the geodynamic processes that formed these cratonic nuclei continue to be debated, there is a general lack of evidence for oceanic-arc/subduction-driven systems akin to those characterising the modern Earth (Rapp et al., 2003) having dominantly operated prior to the Neo-Archean (c. 2.8–2.5 Ga (Condie et al., 2016; Brown and Johnson, 2018)) or, as many authors suggested, even during the whole Archean (Bédard, 2018; Hamilton, 2007). It should be noted that Archean craton records variable processes, some of which produced features similar to Phanerozoic terrains. The geological data testify the occurrence of plate-boundary-like sequences and linear tectonic features (Van Kranendonk, 2010; Kranendonk et al., 2002). However, due to the paucity of continuum-reliable data, it is not possible to provide a definitive answer regarding the global geodynamic processes that were acting (Bédard, 2018; Van Kranendonk, 2010; Bédard and Harris, 2014; Cutts et al., 2014; Van Kranendonk et al., 2007). Archean continental crust has a dome and keel structure in which TTG batholiths intrude through overlying mafic lavas, which records a vertical reorganization of rocks as consequence of the inverse density profile (Collins et al., 1998; Bédard et al., 2003; Chardon et al., 1996). The morphology and spatial distribution of dome and keel structures in Archean terranes is inconsistent with them having formed via subduction(Collins et al., 1998; Bédard et al., 2003; Chardon et al., 1996; Bouhallier et al., 1995; Van Kranendonk, 2010). The metamorphic history of these terrain witness periods of quiescence alternating with thermal events correlating with eruption of high quantities of mafic lavas, during which the whole lithosphere was likely significantly weakened (Bédard et al., 2003; Chardon et al., 1996; Choukroune et al., 1995). Such events correlate with the remobilization of older continental crust, which undergoes partial melting to produce felsic material, alongside potential removal of lithospheric mantle (Bédard, 2006; Zegers and van Keken, 2001; Choukroune et al., 1995). Together, these observations are consistent with a tectonic setting mainly dominated by vertical tectonics, periodically fuelled by magmas derived from anomalously hot mantle sources, such as plumes (Van Kranendonk, 2010; Fischer and Gerya, 2016a). In such a scenario, continental crust would be produced via intra-crustal melting and differentiation and dense mafic residua would be continuously removed via Rayleigh–Taylor instabilities (RTIs) (Wiemer et al., 2018). Owing to the higher T_P, the RTIs would induce decompression melting of the asthenosphere, which would add heat to further assist continued TTG magma generation (Bédard, 2006).

The majority of Archean TTGs feature a distinctive trace element signature (e.g. high La/Yb and low Nb/Ta ratios) that requires their separation from a garnet-, hornblende-, plagioclase-, and rutile-bearing source rock (Moyen and Martin, 2012), such as garnet amphibolite or garnet granulite. These lithologies stabilize in metamorphosed mafic rock types along geothermal gradients of 900–1000 °C/GPa (Palin et al., 2016a; Johnson et al., 2017). Partial melting of mafic crust must therefore have occurred at high-pressure conditions and would produce high amounts of dense residuum, which is not preserved in the Archean record. Thus, a successful geodynamic model aimed at explaining the continental crust production, must be able to predict how the mafic residuum is recycled (Bédard, 2006; Zegers and van Keken, 2001; Jagoutz and Kelemen, 2015). The geochemical signature featured by some Archean rocks resembles an arc signature, prompting the idea that the only means to transport hydrated basalts into the mantle is a subducting plate (Van Hunen and Moyen, 2012; Arndt, 2013; Wyman, 2013). Subduction models could explain how hydrous basalts are transported to great depths, providing a consistent framework to understand continental crust production. On the other hand, geological field data are more consistent with models characterized purely by vertical tectonics (Hamilton, 2007; Bédard et al., 2003; Chardon et al., 1998), which cannot replicate subduction-like geochemical features (Arndt, 2013; Wyman, 2013; Moyen and Van Hunen, 2012).

While the early Earth is known to have been hotter than today, estimates for the absolute mantle T_P during the Palaeo- to Meso-Archean (4.0–3.2 Ga) vary from 1500 °C (Ganne and Feng, 2017) to over 1600 °C (Herzberg et al., 2010). This range is significant, as the bulk of all of the continental crust is thought to have formed during this period of time (Dhuime et al., 2012), and even small differences in mantle T_P have significant effects on the efficacy of different crust-forming processes (Johnson et al., 2013; Sizova et al., 2010, 2014; van Hunen and van den Berg, 2008; Gerya, 2014). Previous geodynamic modeling with a hot (1550-1600 °C) mantle T_P (Johnson et al., 2013) suggested that the eclogitized roots of overthickened mafic crust could have delaminated into the mantle, although they did not consider TTG generation in the same environment. Other numerical studies addressing crust-forming processes did not explore the effect of variable T_P and have not examined changes in composition and density of the mafic crust during partial melting and melt extraction (Rozel et al., 2017; Fischer and Gerya, 2016a; Sizova et al., 2015). Although such studies have predicted the unstable nature of the lithosphere at high mantle T_P, they did not explore the effect that magmatism has on thermal weakening the lithosphere, but instead considered a lithosphere prone to be delaminated and gravitationally unstable (e.g. Fischer and Gerya (2016a) and Sizova et al. (2015) employed a high initial crustal Moho temperature, that implies a weak lithosphere).

Here, we employ a new generation of integrated petrological and thermo-mechanical models to examine the effect of variable mantle T_P on the mineral assemblages produced during heating and thickening of Archean mafic crust, the geochemistry of derivative partial melts, and the removal of crustal melt-depleted residua (see Fig. 1). This modeling replicates a magmatic-dominated geodynamic environment, which is thought to have characterized the pre-plate tectonic Earth (Fischer and Gerya, 2016a; Cawood et al., 2013), and likely involved repeated internal restructuring via cyclical RTI events (Fischer and Gerya, 2016a; Johnson et al., 2013; Sizova et al., 2015; Collins et al., 1998).

2 Methods

2.1 Geodynamic simulations

The geodynamic simulations used a Lagrangian thermo-mechanical finite-element code MVEP2 (Johnson et al., 2013; Thielmann and Kaus, 2012), which solves the 2D fundamental continuum mechanics equations using a extended Boussinesq approximation. The advection of material properties within the numerical domain is handled by a marker-in-cell technique. The fundamental equations are:

$$\frac{\partial v_i}{\partial x_i} = 0 \tag{1}$$

where v is the velocity vector,

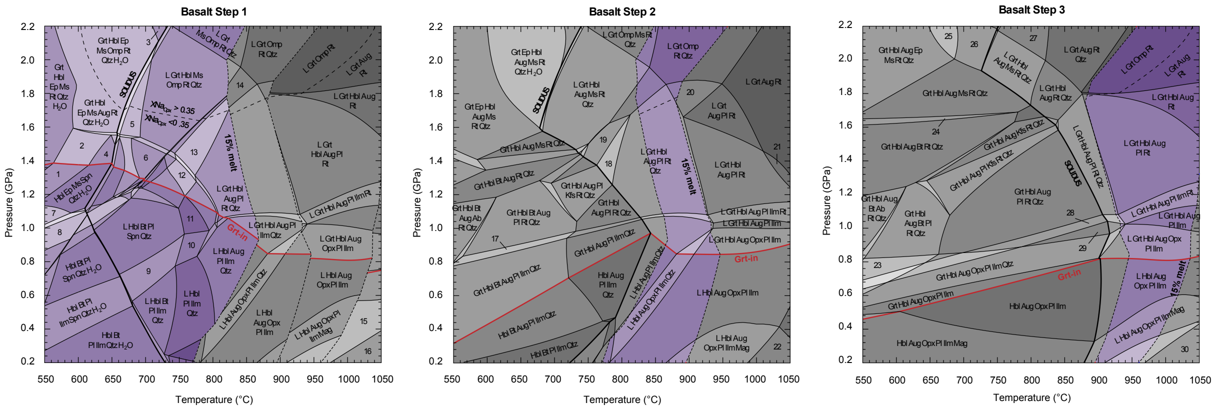

Numbered Field: *1 – Brs Ep Ms Spn Rt Qtz H2O; 2 – Grt Brs Ep Ms Spn Rt Qtz H2O;3 – Grt Hbl Ms Omp Rt Qtz H2O;4 – Grt Brs Ep Ms Spn Qtz H2O;5 – L Grt Brs Ep Ms Omp Rt Qtz; 6 – L Grt Brs Ms Omp Spn Qtz; 7 – Hbl Ep Bt Ms Spn Qtz H2O 8 – Hbl Bt Ms Spn Ab Qtz H2O; 9 – L Hbl Bt Pl Ilm Spn Qtz; 10 – L Hbl Pl Ilm Spn Qtz; 11 – L Hbl Pl Spn Qtz; 12 – L Grt Hbl Aug Kfs Pl Spn Qtz; 13 – L Grt Hbl Aug Kfs Pl Rt Qtz; 14 – L Grt Hbl Di Rt Qtz; 15 – L Hbl Di Opx Pl Ilm Mag 16 – L Hbl Di Opx Pl Mag; 17 – Grt Hbl Bt Aug Pl Ilm Rt Qtz; 18 – L Grt Hbl Aug Pl Kfs Rt Qtz; 19 – L Grt Hbl Aug Kfs Rt Qtz; 20 – L Grt Aug Pl Rt Qtz; 21 – L Grt Hbl Aug Rt; 22 – L Hbl Aug Pl Ilm Mag; 23 – Grt Hbl Aug Bt Pl Qtz; 24 – Grt Hbl Aug Ms Bt Rt Qtz; 25 – Grt Hbl Aug Ep Ms Rt Qtz H2O; 26 – Grt Hbl Aug Ms Rt Qtz H2O; 27 – L Grt Aug Ms Rt Qtz; 28 – Grt Hbl Aug Pl Rt Ilm Qtz; 29 – Grt Hbl Aug Opx Pl Rt Ilm Qtz; 30 – L Hbl Pl Aug Mag*

Figure 1: The purple area in each phase diagram represents the phase relation that can be seen by a rock during a prograde metamorphic between the solidus and the 15% melt modal amount. The red line represents the garnet-in boundary. The leftmost picture represents the first Basalt Step (BS1), the most fertile and hydrated rock. The middle one represents the second basalt step (BS2), while the rightmost is the last Basalt Step (BS3), which is used also for anhydrous intrusions

$$\frac{\partial \tau_{ij}}{\partial x_j} - \frac{\partial P}{\partial x_i} = -\rho g_z \tag{2}$$

where, P is pressure, τ_{ij} is the deviatoric stress component along the considered direction, ρ is density, and g_z is the gravity vector component ($g_z = 9.81\ ms^{-2}$).

$$\rho C_p \left(\frac{\partial T}{\partial t} + v_i \frac{\partial T}{\partial x_i} \right) = \frac{\partial}{\partial x_i} \left(K \frac{\partial T}{\partial x_i} \right) + H_a + H_s + H_r + H_l \tag{3}$$

$$H_s = \tau_{ij} \left(\dot{\epsilon}_{ij} - \dot{\epsilon}_{ij}^{el} \right) \tag{4}$$

$$H_a = T \alpha v_z g \tag{5}$$

C_p is the heat capacity, T is the temperature, and K is the heat conductivity, which is a function of temperature, pressure, and composition (Sizova et al., 2015). H_r, H_s, H_l and H_a are radiogenic heat production, shear heating (eq. (4)), latent heat, and adiabatic heating (eq. (5)) respectively. Latent heat is considered for the melt reactions and is handled by changing the heat capacity and thermal expansivity as function of the melt production (e.g. (Sizova et al., 2015)):

$$\alpha_{eff} = \alpha + \frac{\rho Q_l}{T} \left(\frac{\partial M}{\partial P} \right) \tag{6}$$

$$C_{peff} = C_p + Q_l \left(\frac{\partial M}{\partial T} \right) \tag{7}$$

Where α_{eff} and C_{peff} are the effective thermal expansivity and heat capacity of the partially melted rock, respectively. Q_l is the latent heat. While heat conductivity changes accordingly to an empirical law (Clauser and Huenges, 1995):

$$K(X, P, T) = \left(k_1 + \frac{k_2}{T + 0.77} \right) \exp\left(P k_3\right) \tag{8}$$

where k_1, k_2 and k_3 are empirical parameters that describe how the conductivity changes as function of pressure and temperature (see Table A1).

2.1.1 Rheological Model

MVEP2 is a visco-elasto-plastic code. As a consequence, the deviatoric stress tensor is computed using three constitutive equations that connect it with the strain rate tensor;

$$\dot{\epsilon}_{ij} = \dot{\epsilon}_{ij}^{vis} + \dot{\epsilon}_{ij}^{el} + \dot{\epsilon}_{ij}^{pl} = \frac{\tau_{ij}}{2\eta_{eff}} + \frac{\diamond\tau_{ij}}{2G} + \dot{\gamma}\frac{\partial Q}{\partial \tau_{ij}} \tag{9}$$

where $\dot{\epsilon}_{ij}$ is the total strain rate tensor, the superscript *el,vis,pl* indicate respectively the elastic, viscous and plastic strain rate. $\diamond\tau_{ij}$ is the Jaumann objective stress rate, G is the shear modulus. η_{eff} is the effective viscosity. $\dot{\gamma}$ is the plastic multiplier, Q is the plastic flow potential, which is equal to the second invariant of the deviatoric stress tensor, in a dilatation-free media (Kaus, 2010). We briefly describe the method and numerical implementation, which is explained in more detail in Kaus (2010).

The creep viscosity was computed using the following equations (from Hirth and Kohlstedt (2004)):

$$\eta_{diff} = A_{diff}^{-1} d^{p} exp\left(\frac{E_{act} + PV_{act}}{RT}\right) exp\left(AM\right) \tag{10}$$

$$\eta_{disl} = A_{disl}^{-\frac{1}{n}} \dot{\epsilon}_{II}^{\frac{1}{n}-1} exp\left(\frac{E_{act} + PV_{act}}{nRT}\right) exp\left(\frac{AM}{n}\right) \tag{11}$$

A$_{diff}$ and A$_{disl}$ are the pre-exponential factors for diffusion and dislocation respectively (see Table A1), d and p are the grain size and the grain size exponent, respectively, and n is the stress exponent. E_{act} and V_{act} are the activation energy and activation volume. A is an empirical parameter that describes the porosity weakening associated with melt production and M is the actual volumetric degree of melt after the melt extraction, $\dot{\epsilon}_{II}$ is the second invariant of the strain rate tensor (all parameters used are listed in Table A1). The effective viscosity (η_{eff}) is computed with a quasi-harmonic average between diffusion and dislocation creep viscosity. Brittle rheology was modeled using a Drucker–Prager yield criteria:

$$F(\tau_{II}) = \tau_{II} - C\cos\left(\phi_{dry}\right) - P\sin\left(\phi_{dry}\right)\lambda_{melt} \tag{12}$$

$$\lambda_{melt} = 1 - \frac{P_f}{P_l} \tag{13}$$

F is the yield function, C the cohesion of the material, ϕ is the dry friction angle. λ_{melt} is the weakening factor induced by the melt phase percolating within the rocks during the melt extraction.

At the beginning of the timestep, F is assumed ≤ 0, which implies that the plastic deformation mode is not active:

$$\dot{\lambda} \geq 0, F \leq 0, \dot{\lambda}F = 0 \tag{14}$$

The numerical code computes trial stresses using a viscoelastic rheology, after which the resultant stresses are used to compute $F(\tau_{II})$:

$$\tau_{ij} = 2\eta_{ve}(\dot{\epsilon}_{ij}) + \chi\tau_{ij}^{old} \tag{15}$$

with

$$\chi = \left(1 + \frac{G\Delta t}{\eta_{eff}}\right)^{-1} \tag{16}$$

$$\eta_{ve} = \left[\frac{1}{\eta_{eff}} + \frac{1}{\Delta t G}\right]^{-1} \tag{17}$$

where τ_{ij}^{old} is the deviatoric stress of the previous timestep and Δt is the current time increment. If $F(\tau_{ij})$ is > 0, the code computes a plastic strain rate as such the trial stresses become equal to the stresses predicted by the yield criteria:

$$\tau_{ij} = 2\eta_{ve}(\dot{\epsilon}_{ij} - \dot{\epsilon_{ij}}^{pl}) + \chi\tau_{II}^{old} \tag{18}$$

Eq. 18 can be rearranged:

$$\tau_{Y} = 2\eta_{vep}\dot{\epsilon}_{II} + \chi\tau_{II}^{old} \tag{19}$$

yielding an effective viscosity:

$$\eta_{vep} = \left(\frac{\tau_{Y} - \chi\tau_{II}^{old}}{2\dot{\epsilon}_{II}}\right) \tag{20}$$

where $\dot{\epsilon}_{ij}^{pl}$ is the plastic strain rate, τ_Y is the yield stress and η_{vep} represents an effective viscosity resulting from all the three deformation mechanisms. If the rock is not yielding, the effective viscosity is given by eq. 17, otherwiseis given by eq. 20.

The effective viscosity can vary between a lower and upper threshold values of 10^{18} and 10^{24} Pas respectively. If the effective viscosity yielded by eq. (16) is outside this range, it is automatically set equal to the lower or upper bound. This strategy, which is common for all geodynamic software packages, is imposed for numerical stability as roundoff errors can affect the performance and accuracy of the direct solvers.

2.2 Petrological modeling and melt extraction

2.2.1 Melt extraction

The extraction of melt from each source rock and its emplacement are assumed to be instantaneous over the timescales considered in the geodynamic model, although these processes operate at different rates in the natural environment. While the rate of crystallization for intrusive rocks was modeled according to pluton size, the crystallization of volcanic rocks was considered instantaneous (cf. Sizova et al. (2015)). At each timestep, the melt quantity is interpolated from the phase diagrams (M^E). The interpolated value, however, does not incorporate the extraction event that occurred between two depletion steps. To avoid any melt overproduction, we correct the value using the previously melt extracted, yielding an effective melt quantity ($M*$):

$$M* = M^{E} - \sum_{i=1}^{ts-1} M_{ext}(i) \tag{21}$$

M_{ext} is the volume of melt that has migrated from the source during each extraction event, and ts is the total number of extraction events.

After the computation of $M*$,the code tests whether if this value is higher than $M1$, which represents the minimum melt fraction above which melt can escape from the source. This value is the numerical expression of the critical amount of melt in high-pressure metabasic rocks (Rushmer, 1995). Since the critical amount of melt depends on the deformation, geometric configuration of the minerals and reaction rates, we use a constant value that is varied within the simulations. As a consequence, we neglect some real-world complexities. There are two cases: $M^* < M1$ or $M^* \geqslant M1$. In the first case, M, the effective amount of melt used in the eq. 11, 10 and in the density computation (see below), is $M = M^*$ and $M_{ext} = 0$, in the latter $M = M2$ and $M_{ext} = M^* - M2$. $M2$ is the minimum amount of melt that remains in the source, which controls melt-driven viscous weakening and the buoyancy of the media after melt extraction. As with $M1$, $M2$ depends on many factors that cannot be easily parameterized, and for simplicity we set it as a variable input parameter. After each extraction event, all particles are vertically compacted, reproducing the mass and volume change of the source rocks. After the current melt extracted is computed for each node, we sum the contribution along z direction, yielding an effective thickness of extracted material. This effective thickness is used to apply a compaction to the particles, which creates space for newly generated crust.

The volume of extracted melt is converted into extrusive or intrusive crust, whose proportion is defined by the parameter I_R ($= V_{intrusion}/V_{Totmelt}$) which is an non-dimensional quantity that ranges from 0 to 1 (0% to 100 %). The intrusion is emplaced where the maximum ratio between the fluid over-pressure and effective viscosity is achieved:

$$div(Crust) = \frac{P_{liquid} - P_{solid}}{\eta_{eff}} \tag{22}$$

$div(Crust)$ is the ratio between fluid over-pressure and effective viscosity, P_{liquid} is the hydrostatic liquid pressure computed accordingly to the melt density, while P_{solid} is the lithospheric pressure. The depth of emplacement depends on the density of the melt and on the rheology of the crust and it changes according to the dynamics of the system.

2.2.2 Petrological modeling

Petrological modeling of metamorphism and partial melting in Archean crust was performed in the Na_2O–CaO–K_2O–FeO–MgO–Al_2O_3–SiO_2–H_2O–TiO_2–O_2 system using *THERMOCALC* version 3.45i (Powell and Holland, 1988), internally consistent thermodynamic dataset ds62 of Holland and Powell (2011), and the following a–x relations: epidote, olivine (Holland and Powell, 2011), silicate melt, augite, hornblende (Green et al., 2016), garnet, orthopyroxene, biotite, chlorite (White et al., 2014), magnetite–spinel (White et al., 2002), ilmenite–hematite (White et al., 2000), Cbar-1 plagioclase, K-feldspar (Holland and Powell, 2003), and muscovite–paragonite (White et al., 2014). All calculations utilized the initial bulk-rock composition for an average LILE-enriched Archean tholeiite (EAT, ref. Condie (2003)), which has been suggested on major- and trace-element geochemical grounds to be the most suitable source rock for Archaean TTGs (Moyen and Martin, 2012; Martin et al., 2014).

The bulk chemical composition of a rock imparts a primary control on the phases that stabilize as a function of P–T conditions, solidus topology, and ultimately on their rheology, density and radiogenic heat productivity. All together these effects have first-order controls on the dynamics of the target system. To encompass such complex feedback, we parameterized the chemical evolution of the rocks by discretizing it, and assuming that it compositionally evolves only as function of melt loss. We averaged the chemical composition of the residuum along the same melt-fraction isoline to produce new phase diagrams. Such chemical evolution is matched to individual particles that carry all petrophysical information and are advected within the numerical domain.

All particles have their own identification number and rock type. Rock type connects the particles with the petro-thermo-chemical properties of the modeled lithotype, and with phase diagrams. To enforce the chemical composition evolution, the rock type of a particles can change if the total melt extracted exceeds a threshold value, *M3* (see below and Supplementary Material Fig. A12). We do not explicitly deal with reaction lines; the residual composition and associated phase diagram is computed beforehand (see below for further details). Albeit more sophisticated and correct methods exist and have been already applied (Rummel et al., 2018; Riel et al., 2018), they require more computational cost and resources, that make them currently unsuitable for obtaining statistically significant results for the Archean dynamics. Radiogenic heat productivity is assumed to diminish at each depletion step and it discretely varies within an interval whose extremes are the inferred Archean and the modern-day values for the respective lithologies (e.g. Mantle radiogenic heat production interval spans from 0.022 to 0.066 $\mu W m^{-3}$ and each evolutionary stage entails a decrease of 0.022 $\mu W m^{-3}$).

Petrophysical properties of metamorphic rock types, such as whole-rock density, individual melt and residuum density, volumetric melt fraction (M^E) and constituent mineral compositions and proportions, were calculated using *THERMOCALC* and used as input data for geodynamic modeling. Given that melt-loss is an open-system process, M^E was adjusted during each extraction event; consequently, this value differs from M (effective volumetric degree of melt). A unique phase diagram was thus calculated for each rock type (e.g. Basalt Step 4 and Mafic Intrusion). All petrophysical properties of unmelted protolith, extracted melt, and depleted residuum (e.g. density) were calculated for each node as a function of pressure, temperature, composition (X) and M:

$$\rho_{eff}(X,P,T,M) = M\rho_{melt}(X,P,T) + (1-M)\rho_{solid}(X,P,T) \tag{23}$$

where $\rho_{melt}(X,P,T)$ is the density of the melt, $\rho_{solid}(X,P,T)$ is the density of the solid fraction. Since we do not consider continental crust reworking, we do not use phase diagrams for the felsic crustal rocks, and its density is computed by using a simple parameterization:

$$\rho_{felsic}(P,T) = \rho_0\left[1-\alpha(T-T_0)\right]\left[1+\beta(P-P_0)\right] \tag{24}$$

where ρ_0 is the reference density (2650 kg m^{-3}), T_0 and P_0 are respectively the reference temperature and pressure.

The initial mafic crust was assumed to be LILE-enriched Archaean tholeiite (EAT) derived from a primitive undifferentiated dry mantle (Condie, 2005). Phase diagrams were calculated for specific bulk-rock compositions depending on the number of times that melt had been extracted, as follows:

1. Mantle rocks: phase equilibria for the asthenospheric mantle source rock were calculated using the fertile peridotite (MFP) composition presented by Johnson et al. (2013) –the a–x relations and thermodynamic datasets are outlined therein –, and a total melt extraction threshold of 25% (i.e. M3 = 25%) was applied. Following melt loss, the complementary effective bulk composition for lithospheric mantle (also taken from Johnson et al. (2013)) was termed mantle depletion step 1 (MDS1). During our systematic analysis, the rheological flow law of MFP was changed to simulate stiffening of the mantle as consequence of melt extraction. The stiffening of the mantle is modeled by increasing the pre-exponential factor of diffusion and dislocation creep by one order of magnitude (see Table A2 for further information). MDS1 was allowed to

Table 1: Composition of basalts used in geodynamic models from which TTG magmas were derived All the compositions are listed as mole % oxide. (*) Basalt Step 4 has the same phase diagram of Basalt Step 3, but, after the extraction, the predicted composition is the one listed

Rock Types	H_2O	SiO_2	Al_2O_3	CaO	MgO	FeO^{Tot}	K_2O	Na_2O	TiO_2	O
BS1/BT2	6.830	49.693	8.992	9.214	10.205	9.814	0.442	2.628	1.125	1.058
BS2	4.443	47.975	9.118	10.330	11.775	11.238	0.227	2.373	1.304	1.226
BS3	2.329	45.712	9.198	11.557	13.489	12.738	0.102	1.947	1.509	1.419
BS4(*)	1.163	43.856	9.173	12.879	14.824	13.380	0.044	1.284	1.751	1.647

melt, and if the incremental melt extraction exceed 45 % of total melt extracted the rock type and phase diagram was changed for the last time; MDS2 was not allowed to melt again, meaning that no further chemical evolution of the mantle took place in our model.

2. Crustal rocks: phase equilibria for mafic crustal units were computed using *THERMOCALC* 3.45 (Powell and Holland, 1988), using the Holland and Powell (2011) dataset (ds62) and the a–x relations of Green et al. (2016) as outlined above (see Figure 1). A phase diagram for undepleted EAT (BS1) was utilised as a baseline reference system from which subsequent pseudosections were derived. A melt-extraction threshold (M3) of 15% was applied for these crustal lithologies (following Rushmer (1995)) , with sequential melt loss producing increasingly depleted source rocks and melts termed basalt step 2 (BS2), basalt step 3 (BS3), and basalt step 4 (BS4) (Palin et al., 2016a), the last of which has an anhydrous residue and thus no longer produces significant quantities of melt. Bulk compositions for melt-depleted lithologies were calculated using the read-bulk-info matrix function, which was adjusted to account for 15% relative melt loss at the P–T conditions of melt extraction calculated on the 15% melt proportion contour from the source lithology. This threshold was chosen owing to it representing the upper limit of favorable conditions for efficient melt segregation and escape from partially melted mafic rocks, as determined experimentally for garnet amphibolites by Rushmer (1995). While such a value is affected by several factors (i.e. strain, temperature, grain size, and shape), it represents a defensible cut-off for the lithologies and general P–T conditions of melting observed in this simulation, which match those used during the experiments of Rushmer (1995).

Phase diagrams for residual lithotypes used these critical melt fractions, within the perspective of minimizing the number of phase diagrams to be discretized while being able to capture the first order effect of the chemical composition evolution. We use a lower melt threshold (*M1*) to incorporate all kinds of magmatic processes that may occur during the extraction. All melts generated are termed “felsic” and either erupt as lavas or stall as intrusions in the middle to lower crust. These felsic melts can be derived from BS1, BS2, BS3 or BT2. The bulk compositions used for modeling are given in Tab. 1. The effusive basalt associated with the mantle phase MDS1 has a different composition but it is modeled using the same phase diagrams of the BS1 as most metabasalts have similar melting evolution (Palin et al., 2016b). We differentiate it from the other kind of basalts (Basalt Type 2, BT2) to track the amount of basalt coming from a depleted mantle source. It produces small amount of felsic melt, and then is converted into a dense residue without following the path assigned to the EAT basalts. In any case the amount of BT2 is negligible respect to the EAT protoliths, as it does not contribute significantly to overall felsic magma production.

In each timestep both intrusive and effusive crust produced by the mantle derived melts. Intrusive mafic systems are complex and feature internal differentiation, producing composite suites of rock dominated by dry gabbro and ultramafic cumulates (Cox, 1980). Such complexity cannot be handled by the current melt extraction parameterization. Therefore, we choose to simplify it introducing an effective dense unfertile material that is emplaced as intrusive body within the lower crust or as underplated mafic materials. We assume that these composite intrusions feature a high magnesium number and to model these dense bodies we employ the same phase diagram of the Basalt Step 3, without melting, of which composition resembles Archean picrites. Intrusion as possible source of the felsic crust was not considered to avoid over-estimation of felsic material and preferring to investigate the effects of the evolution of the hydrous mafic crust. In previous work (Sizova et al., 2015) the dry underplated basalt have been considered as available source of felsic crust as well. However, the bulk of continental crust produced in their simulation were originated by dry intrusions, and it has been interpreted as intermediate material (i.e. andesite). However intermediate rocks are rare in the Archean terrains (Anhaeusser, 2014), and we choose to focusing only in the mafic protolith that could really bear TTGs. However, the density of these intrusion is higher than a normal dry basalt, so in order to check if the prediction of such approach is correct we performed a test using the anhydrous basalt employed in Johnson et al. (2013), yielding a similar results.

Our approach has an important limitation related to the dehydration reactions. Our modeling approach cannot handle the dehydratation reaction and the magmatic processes. All the mafic crust phase diagrams have computed assuming that the BS1 is always minimally saturated in water at the solidus. This approach guarantees that the rocks were always saturated during the prograde metamorphism and it implicitly assumes that the rocks are always fully hydrated. In any case, with the exception of perfectly anhydrous, metabasalt all partially or fully hydrated metabasalts will produce the majority of their melt at similar conditions across the amphibolite-to-granulite boundary (Palin et al., 2016a). So, our numerical experiments represent the most favourable conditions to produce continental crust in a vertical setting.

In summary, the compositional evolution starts with a fertile peridotite (MFP) that melts as consequence of the increase of T_P due to mantle radiogenic heat production and decompression. After 25% of melt extracted the mantle fertile peridotite evolves toward the Mantle Depletion Step 1 which could produce new basalts with different composition (Basalt Type 2). If the MDS1 and the initial Lithospheric Mantle experience 20% melt extraction it is converted into Mantle Depletion Step 2 and is considered fully depleted. The product of MFP is dense mafic intrusion (Intrusion) and tholeiitic basalts (Basalt Step 1). The hydrated basalt is buried and heated from below, and if it melts, it generates high silica melt, that is extracted generating Felsic Crust. Basalt Step 1 evolves towards the Basalt Step 2 (after 15% melt extraction), which eventually melts again producing new felsic crust, and evolving towards the Basaltic step 3 and then to Basaltic step 4. If total melt extracted is higher than the respective threshold (15, 30, 45% respectively) the phase diagram and rock type are changed.

2.3 Results

Initial Setup Our baseline scenario (Reference model) is represented by a two-dimensional numerical model comprising numerous layers (see Supplementary Material (Gerya and Meilick, 2011; Kaus et al., 2010; Gerya et al., 2008; Ranalli, 1995), Figure A1). With increasing depth, this comprised an 80 km thick lithosphere with a 24 km thick crust, of which the uppermost portion is composed of 16 km of hydrated (fertile) basalts (Basalt Step 1, BS1) overlying 8 km of anhydrous (unfertile) basalt/gabbro (Intrusion). The underlying lithospheric mantle is considered partially depleted, consistent with the predicted Archean residual mantle composition (Johnson et al., 2013; Herzberg et al., 2010). The asthenospheric mantle is composed of anhydrous fertile peridotite (MFP). The mineral assemblages (with or without melt) that would be stable at each P–T conditions through this profile were calculated using thermodynamic phase equilibrium modeling (see Methods), alongside bulk-rock physical properties (e.g. density). These phase assemblages dynamically evolved with simulation time and were re-calculated at each node as P, T, and bulk composition constraints changed.

The lithosphere featured an initially segmented geotherm: a crustal segment, with a Moho temperature (T_{Moho}) of 800 °C, which produced an apparent geotherm of 1000 °C/GPa, and a lithospheric mantle segment, with a T_P at the base of the lithosphere of 1550 °C. This reference model assumes effective melt weakening (λ_{melt} = 0.01), which reduces the brittle strength of the lithosphere during melt-loss events (Sizova et al., 2015). As the hydrated basalts (BS1) are buried, they partially melt, with phase equilibrium modeling used to calculate the compositions of generated magmas. Such melts are high-silica magmas that can be extracted to form felsic crust (see Methods). Once the calculated volume of melt generated reaches a critical threshold, accumulated melt is extracted from the system. As this changes the bulk composition of the system, a new phase diagram was calculated to determine the stable mineral assemblage following melt loss (see Fig. 1). Such stepwise melt-loss and depletion was permitted to occur up to three times, such that melt was extracted from each basalt when its cumulative total reached 15%, after which the rock is considered fully melt-depleted (Basalt Step 1 to Basalt Step 4, BS1-4). Likewise, the asthenospheric mantle was allowed to change phase diagrams two times when the total melt extracted reached the two thresholds values (25% and 45%). These stages are denoted MFP to Mantle depletion step 1-2, MDS1-2. Extracted melt is either converted into hydrated basalt (BS1) if extruded, consistent with an Archean subaqueous environment (Kump and Barley, 2007), or as anhydrous basalt/gabbro if intruded.

MDS1 produces small amounts of melt that generate a distinct basalt (BT2) to highlight the difference between the basalt that is produced from a more fertile source with respect to those produced by a partially depleted one. BT2 undergoes a single stage before being converted in unfertile residue (see Methods). Initially, 50% of the mafic melt produced was assumed to stall during ascent through the crust and form intrusions. While this is lower than the average noted for the present-day Earth (80–90% intrusion)(Crisp, 1984), this ratio is highly variable between geological environments; for example, plume-related magmatism is typically characterised by 66% of magmas forming intrusions (Crisp, 1984; White et al., 2006), and this ratio can evolve with time depending on the rheological structure of the crust changing during cooling (Rubin, 1993). In our modeling, extrusion is assumed to occur via dike formation, with the diking efficiency controlled by the rheological structure of the crust (Rubin, 1993). In most simulations, we employ a conservative scenario in which the eruptive efficiency remains constant throughout the simulation, which mimics stiffening of the crust due to eruption of high amounts of mafic lavas (Rubin, 1993). This ratio produces a strong crust, which promotes diking and efficient effusive volcanism, consistent with the thick volcano-sedimentary sequences in Paleo-Archaean terrains (e.g. the East Pilbara craton (Hickman and Van Kranendonk, 2012)).

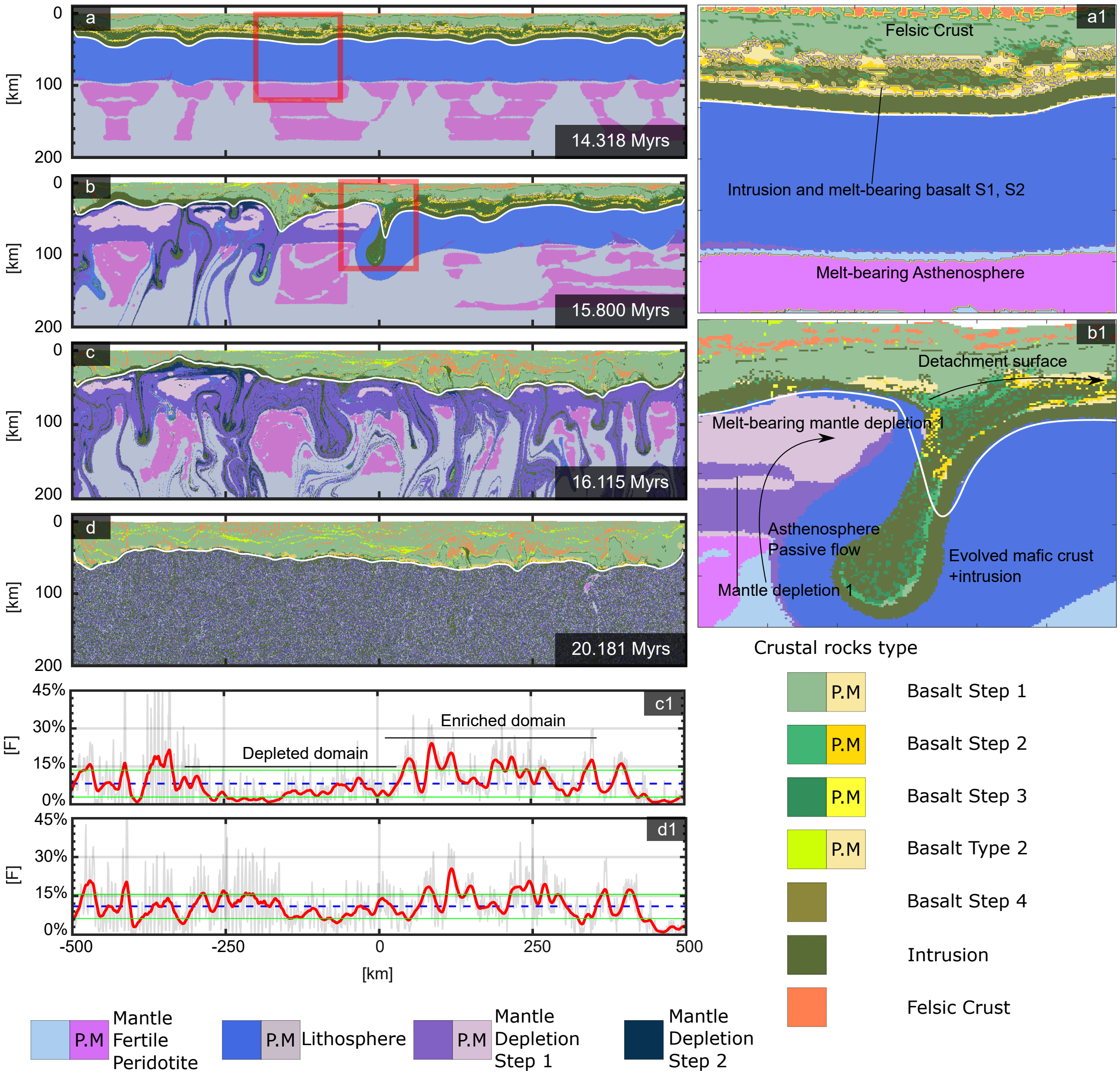

Figure 2: **Temporal evolution of the reference simulation (T_P = 1550 °C, T_{Moho} = 800 °C, λ_{melt}=0.01,ϕ_{dry}=30° and an intrusive/extrusive ratio = 50%.** Three characteristic evolutionary stages are shown: **a):** incubation, **b-c):** dripping and intraplate deformation sub-stage and **d):** steady state stage. **a1** and **b1** are related respectively to **a** and **b** and are enlargement of the area surrounded by the thick rectangular boxes. **c1** and **d1** are the monodimensional profile, in which F, the relative amount of felsic crust, is plotted against the horizontal direction. The red line is the moving average of the raw data - grey lines in the same plot- with a window of 20 km, the blue line represent the global average and the two green lines represent 1 STD of the data.

Reference Model: The reference model exhibited three main stages: an incubation stage, a drip stage, which features strong intraplate deformation, and a steady-state stage (Fig. 2). During the *incubation stage* (0–14 Myrs), the asthenosphere undergoes partial melting as a consequence of the high T_P. Melt is extracted from the uppermost partially-melted area, and the mantle depleted residue sinks, generating small convective cells within the partially molten area of the asthenosphere (see Fig. 2a) . These convection cells locally induce decompression melting that generates further mafic intrusive and eruptive material. Heat is mainly provided to the crust by the emplacement of stalled magmas and generates warm geotherms, consistent with those recorded in Meso-Archean terranes (Brown, 2007). By contrast the radiogenic heat production has a smaller effect at this stage due to the paucity of relatively radiogenic felsic crust, which has been shown to play a major role for the generation of significant amount of continental crust (Bodorkos et al., 2006). Burial of hydrated lavas following continued eruptions stabilizes amphibolite, garnet amphibolite, and garnet granulite with depth (Figs. 1 and 3), which form at approximately 16 km, 30 km, and

36 km depth in the crust, respectively. Representative densities of each lithology along these geotherms comprise 3050–3150 kg m^{-3}, 3250–3300 kg m^{-3}, and 3450–3550 kg m^{-3}, respectively. Both garnet amphibolite and garnet granulite melt to produce TTG-like magmas with major and trace element signatures matching Archaean examples. The burial is mainly controlled by the distribution of the magmatic activity, that is focused beneath small convection cells in the asthenosphere. The mafic intrusions heat up the crust, driving the production and extraction of felsic magmas from amphibolite/garnet-amphibolite (hydrated metabasalt), and leaving a complementary mafic residuum. This process allows RTIs to develop (Fig. 3b).

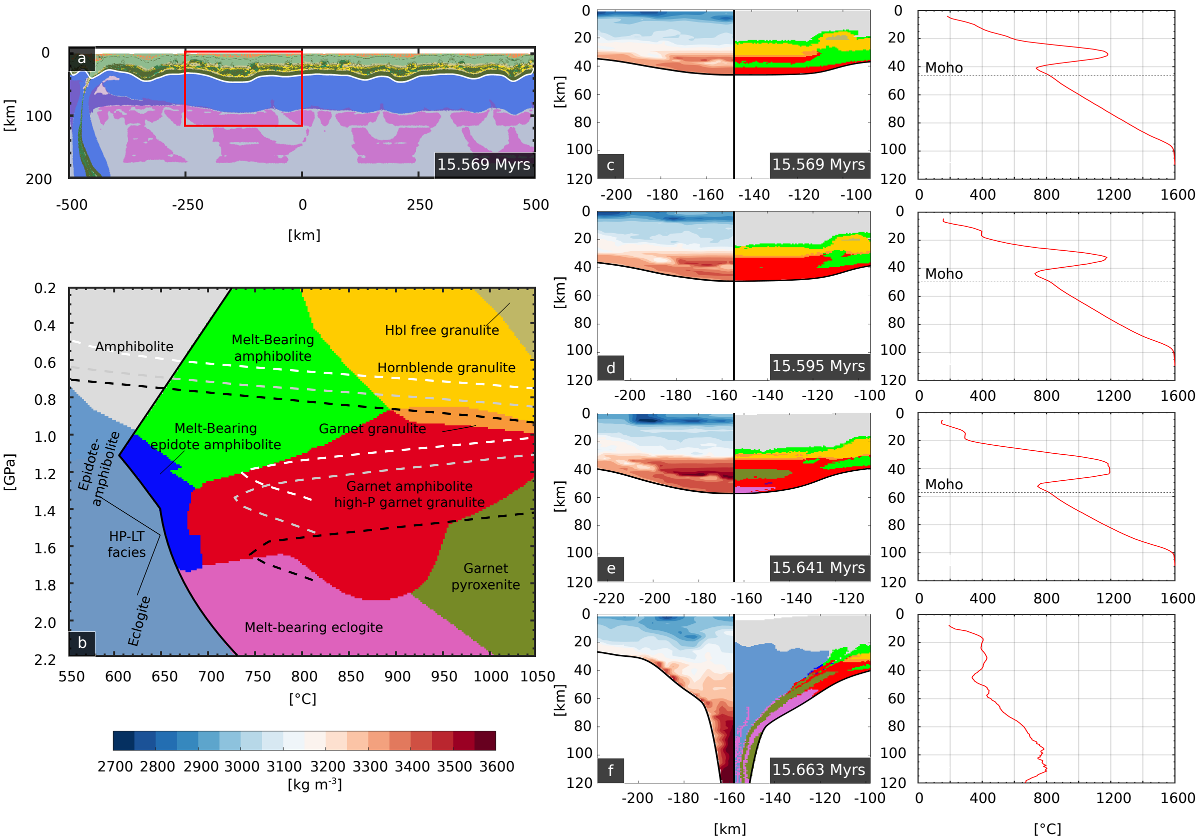

Figure 3: **Petrophysical architecture of a drip**. **a):** The reference scenario in the embryonic stage of drip formation; **b):** Petrological diagram showing rock types stable at different pressure–temperature conditions within the drip, taken from Palin et al. (2016a). Colour coding for rock type is used for subsequent plots. The dashed lines represents the geotherm along the axis of the drip (white, grey and black refer respectively to **c**,**d** and **e** sub-panels); **c):** Embryonic pre-drip stage when intrusion of magma begins to heat the lower crust. Rock types at this depth are dominantly amphibolite and garnet amphibolite and have densities of around 3200–3400 kgm^{-3} ; **d):** Densification of lower crustal units occurs soon after initial drip embryo development. The density of the lower crust is increased with respect to the mantle, due to mafic residue left over from extraction of felsic crust; **e):** Minor eclogite-facies rocks form at the base of the crust as a result of thickening and drip development; **f):** Dripping eventually occurs owing to gravitational instability.

Partial melting of amphibolite/garnet-amphibolite followed by melt extraction generates large volumes of negatively buoyant mafic/ultramafic residue (Fig. 3), which forms drips in thickened crust (Fig. 3b). Increased pressure in these regions acts to further stabilize garnet and destabilize feldspar, causing their sagging bases to transform to eclogite upon reaching pressures of ~1.8 GPa, (Fig. 3c-d). Further melting of these relatively dry eclogitic residual rocks is limited, consistent with observations that TTGs derived from eclogite-facies precursors represent minor (<10%) components of all Archean terrains (Moyen, 2011). During the incubation stage, the crust is weakened due to two factors: continuous emplacement of mafic intrusions that heats the lithosphere, and the production of mafic (high-density) residuum which destabilizes the entire lower-middle crust (see Fig. 3, Fig. 4b, where it is shown the density and viscosity field respectively).

The *dripping stage* (~14-22 Myrs) starts as soon as the first drip nucleates, as shown in our simulations at the left-hand side of the numerical domain (Fig.4). The relatively high viscosity of the lithosphere enables the transmission of the gravitational pull force to the whole crust, which yields plastically due to weakening by magma percolation.

The formation of drips allows asthenospheric mantle upwelling, which produces mafic melt that intrudes into and further weakens the crust. The crust is rafted apart by the asthenosphere and its horizontal displacement facilitates the nucleation of adjacent RTIs, enhancing the local compression associated with their development (Elkins-Tanton, 2007; Beall et al., 2017) (see Fig. 4). Local vertical stretching further increases the density of residual rocks (see Fig.3). The rapid evolution of the drips drags in the lower–middle crustal rocks from the adjacent area, whose migration locally induces intraplate extension near the drips (see Fig. 4). The viscosity of the crust is sufficiently high to couple the buoyant mafic crust and the dense residual rocks. Brittle deformation controls the amount of material that can be dragged by the drips; since during the incubation-dripping stage the friction angle is decreased by the percolating mafic magmas, large amounts of composite material founders into the mantle (felsic and hydrous components). The dripped composite crust sinks and stalls at the bottom of the model, generating thermal/compositional anomalies.

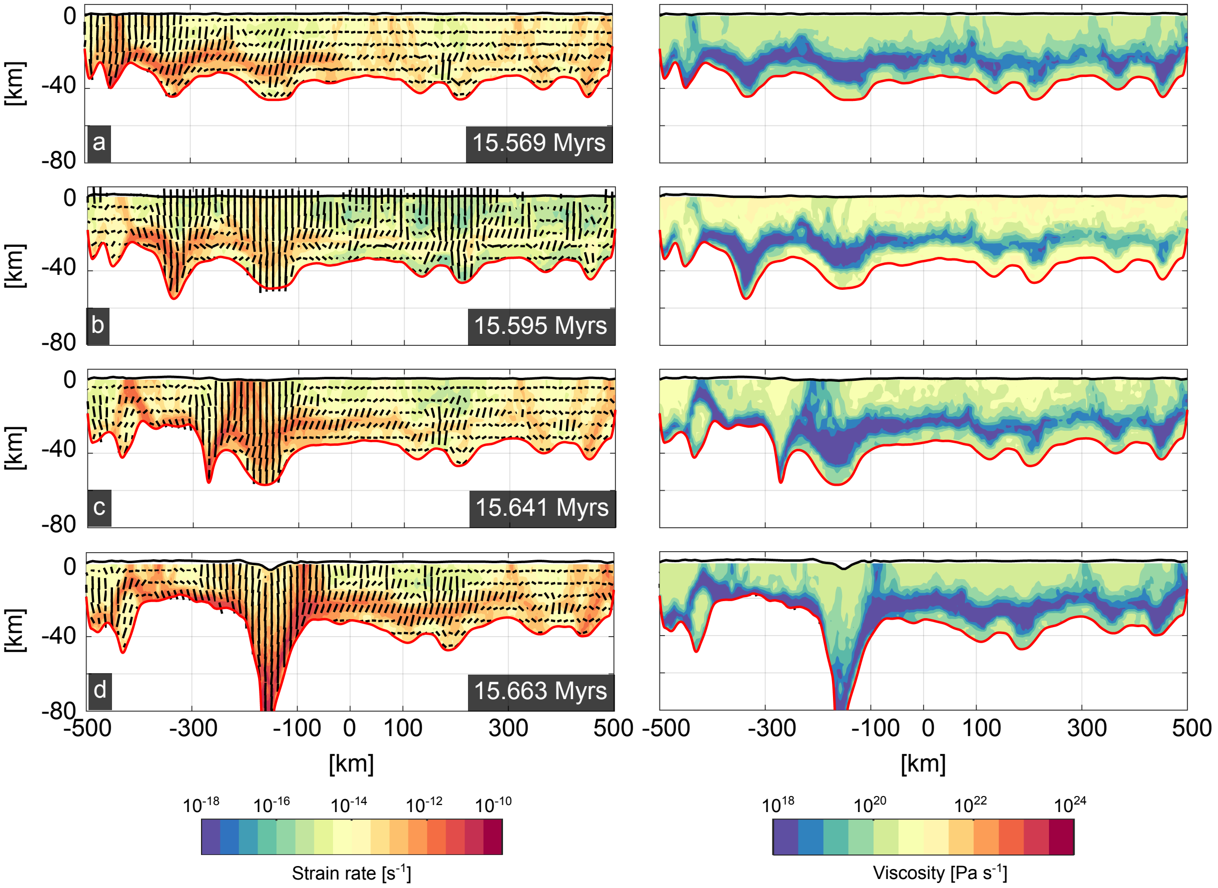

Figure 4: **Strain rate and viscosity field** The left and right column represent strain rate and viscosity field, respectively, of the crust. The thick black and red lines are the topography and the Moho respectively. At the top of the strain rate field the minimum axis of the stress tensor (σ_3) is shown. **a):** After the first drip, the stress is propagated through the entire section of the crust, which concurrently helps to develop the adjacent drip and generates short lived crustal scale shear zones in the right part of the box; **b):** The second drip starts enucleating, dragging the adjacent material. The stress field rotates generating extension in the left area and dragging dense material from the middle crust of the adjacent area; **c):** After the delamination of the second drips, the asthenosphere upwells to fill the empty space left, generating melting that further weakens the crust, triggering a symmetric extension that facilitates the development of the third instabilities (whose density and metamorphic evolution is shown in Figs 2,3); **d):** The extension propagates, assisted by drag force exerted by the asthenosphere and by the complete development of the third drips.

The prolonged stretching of the crust generates narrow 2D rift-like structures in which asthenosphere penetrates the crust. These processes result in a lateral variation in crustal structure coincident with felsic composition anomalies, which strongly resemble observed Archean dome and keel tectonic architecture (Fig. 2) (Hamilton, 2007; Collins et al., 1998; Bouhallier et al., 1995). The drip stage lasts 8 Myr, during which the proportion of felsic components increases to an average volume of 12%, and up to 25% in the stretched region (with a production rate of 696 $km^3 km^{-1} Myrs^{-1}$). Since significant amounts of cold volcanic crust are erupted at the surface, the resulting geotherm has a cold upper crust and hot lower crust, whilst the mantle T$_P$ cools significantly by around 120 °C, producing a new ambient temperature of 1430 °C (see Supplementary Material, Fig. A2). Importantly, the asthenospheric mantle becomes well mixed with residual and intrusive crustal components, which could allow partial hydration of the mantle that could trigger further melting (Bédard, 2006; Bédard et al., 2013); however, this processes is not considered here. Intraplate deformation associated with the dripping stage is analogous to that proposed for the disaggregation of the Superior Craton, with our model providing a mechanism through which Archean lithosphere is weakened and rafted apart by mantle processes (Bédard and Harris, 2014; Bédard, 2018).

As a consequence of the dripping stage, the mantle cools, reducing its fertility, and its viscosity increases, making convection less efficient. While the crustal geotherm is cold as a consequence of the intense and fast magmatic thickening, resulting in a stiff crust (akin to the heat-pipe model (Moore and Webb, 2013)). These conditions inhibit dripping, which is confined to the lowermost crust. These lower crustal drips are small compared to the initial one and have only minor geodynamic effects. The compositional evolution of the crust reaches a *steady-state stage*, in which the felsic crust proportion steadily increases, concurrent with slow minor dripping of the mafic residuum. During the steady state stage, the mantle magmatic activity is no longer continuous and magma production is associated with small mantle upwellings triggered by the old dripped material that has become buoyant as consequence of its thermal equilibration. The original lithospheric mantle has been completely eroded, which makes the new crust virtually unsubductable (Bédard, 2018).

Sensitivity to the initial rheological structure and intrusive/effusive ratio: The initial rheological structure of the lithosphere affects the evolution of the numerical experiments. Increasing T_{Moho} weakens the crust and lithosphere because the respective geothermal gradient increases, and the viscosity decreases as a result. If the viscosity is low, the dense material in the lower-middle crust is fully decoupled from the buoyant supracrustal units. As a consequence the gravitational pull exerted by the RTIs is not effective, and the intraplate deformation observed in the reference experiment is suppressed, resulting in a lateral thickened and compositionally homogeneous crust (see Supplementary Material Fig. A3 and Fig. A4). Low brittle strength values ($\lambda_{melt} < 0.1$, $\phi_{dry} < 15$ °) for the lithosphere favour intraplate deformation, drip formation, significant mantle cooling, and recycling of large amounts of variably-hydrated mafic and felsic material into the mantle (Fig. 5 and Supplementary Material, Fig. A6). A strong lithosphere, on the other hand, has the opposite effect and results in a coherent lithosphere dominated by magmatic processes (see Supplementary Material, Fig. A5).

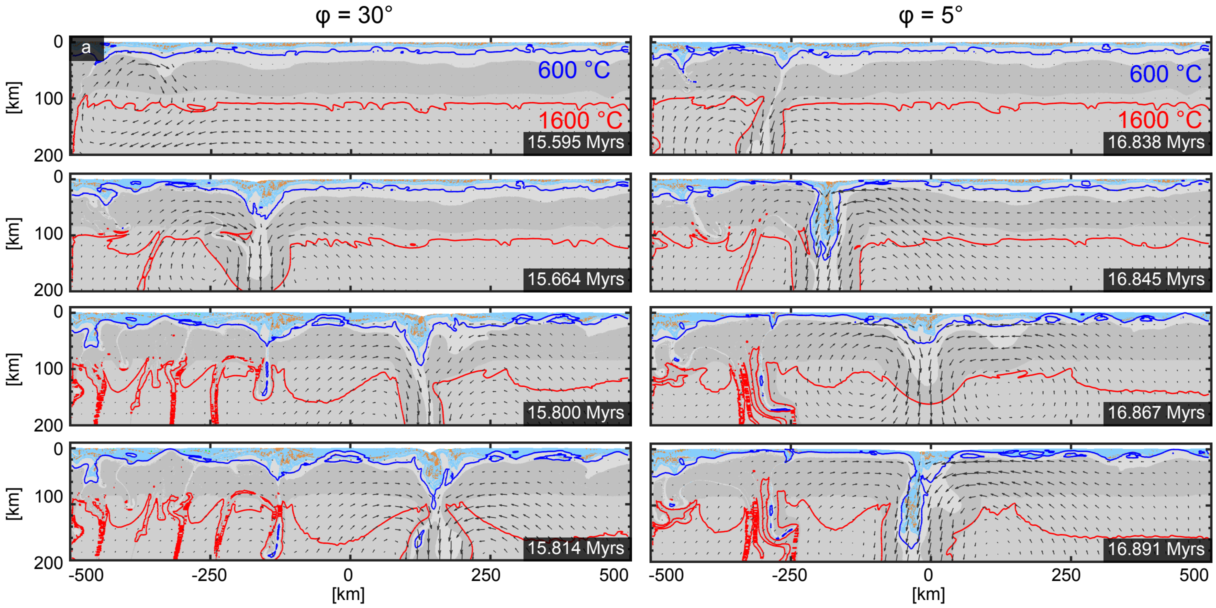

Figure 5: **Effect of the strength of the crust on bringing hydrated material in the mantle.** In these simulations, blue colours represent newly hydrated crust, orange newly formed TTG, and grey the lower crust, mantle lithosphere and asthenosphere. The red and blue lines represent respectively the 600 and 1600 $^{\circ}C$ isotherms. Simulations are performed for a friction angle that is **a)** similar to that of dry, intact crust, **b)** represents that of a hydrated and damaged crust. Other parameters are the same as in the reference test (i.e. T_{Moho}=800 °C, λ_{melt}=0.01). Decreasing the friction angle results in a thinner crust and promotes periods of horizontal tectonics during which significant volumes of hydrated crust are transported into the mantle.

The variation in the ratio between plutonism and volcanism does not significantly affect the four-stage evolution observed in the reference scenario unless more than 80% of mantle-derived magmas stall during ascent, in which case the total crustal recycling process is completed within 2 Myr. Retaining higher volumes of partial melt in the mantle (2% rather than 0.2%) decreases the timescales of the incubation stage (see Supplementary Material, Fig. A7 and Fig A8 which show the crustal thickness evolution).

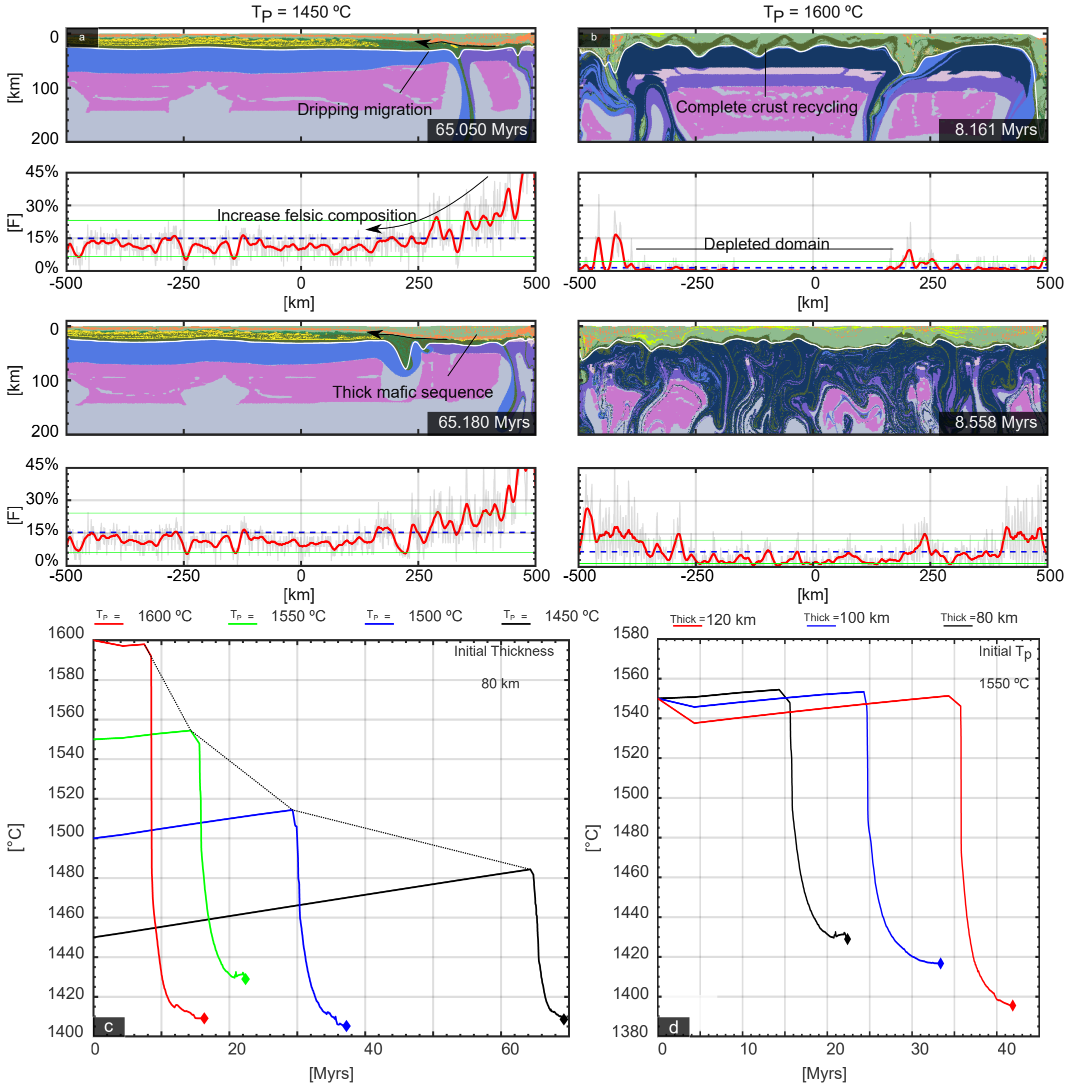

Figure 6: **Effect of dripping instabilities on underlying mantle potential temperature (T_P).** All the compositional plot use the same legend as in Fig. 2. **a):** Evolution of the dripping stage for an initial T_P of 1450 °C. A relatively low initial T_P prolongs the incubation stage, promoting the generation of significant volumes of felsic crust and associated dense, mafic residuum. Dripping is triggered by negative buoyancy and rheological weakening induced by the intrusion of hot mafic magmas; **b):** As in (a), but with an initial T_P of 1600 °C. Here, enhanced dripping causes the primitive crust to be completely recycled, regardless of the amount of felsic crust generated at any location. Multiple rifts develop simultaneously and enhance destruction of the primary mafic crust and derived felsic crust produced during the incubation stage; **c):** Temporal evolution of average T_P for experiments with different initial T_P values (red, green, blue and black lines represents experiment with an initial T_P of 1600, 1550, 1500 and 1450 °C respectively); **d):** Temporal evolution of experiments featuring the same T_P of 1550 °C, but with different lithospheric thickness (black is 80 km, blue is 100 km and red is 120 km). In all cases, the asthenospheric mantle T_P decreases rapidly as a result of addition of colder lithospheric material via dripping instabilities.

Effect of T_P: The duration of the incubation stage is inversely proportional to T_P. For example, at T_P = 1450 °C, the initial incubation stage lasts over four times longer than the reference scenario (65 Myrs compared to 14 Myrs). All dense lithologies (i.e. dry intrusion and mafic dense residuum, BS2-4) act in tandem to generate gravitational instabilities. The production of residuum facilitates the process by increasing the effective thickness of negatively buoyant material and favouring gravitational instabilities under a wide range of thermal conditions, especially at lower T_P. Before the onset of the drip instabilities, the ratio between new hot mantle-derived intrusions and mafic residuum is approximately 1:1, with the former being rheologically weaker and denser than mafic lower crust. This ratio grows in favour of the dense residuum as function of the T_{Moho}, the initial thickness and inversely respect with T_P. The amount of dense residuum required to trigger the drip instabilities in the reference scenario is 4 km (effective thickness, 12% of total crust thickness) with roughly the same amount of new dense intrusions. If the T_P (1450 °C) is lower, the amount of residuum is 8 km, meanwhile the amount of intruded material is halved compared to the reference scenario. The average volume of hydrous basalt that has depleted before the onset of the dripping stage thus gives a measure of the compositional evolution of the crust (see Supplementary Material and Fig. A2), as its maximum value represents how much of the hydrated crust has been converted while the crust was stable.

The average amount of metabasalt that must be converted into dense mafic residuum to trigger dripping instabilities monotonically increases with decreasing T_P (from 20% at 1550 °C to 72% at 1450 °C). Drips induced by such processes buffer the upper mantle T_P, such that localized mantle "cool spots" may have been present during the Archean associated with sites of TTG-like magma generation that immediately precede the drip (Fig. 6). Higher initial mantle T_P (>1550 °C) promotes drip tectonics and total recycling of the crust without requiring large amounts of mafic dense residuum. The amount of intraplate deformation depends on the amount of extracted mafic melts, and effectively ceases for mantle T_P values less than 1500°C.

Crustal production rates and melting conditions: The average amount of continental crust produced in these simulations during the incubation stage is 350± 280 $km^3 km^{-1} Myrs^{-1}$ while during the dripping stage the average production rate is 728± 254 $km^3 km^{-1} Myrs^{-1}$ (see Supplementary Material, Fig. A9). The continental crust production rate during the dripping stage does not correlate with the initial T_P, which only controls its rate of production during the incubation stage. The processes that control dripping-assisted continental crust production is mainly ruled by the feedback between asthenosphere decompression melting and the RTIs . The production of mafic melt is limited by the mantle depletion, thus the independence from the T_P is related to the decreases of mantle fertility and by the extreme mantle cooling rate.

The P–T conditions at which hydrated mafic crust experienced melting varied substantially during each experiment. In general, during the incubation stage TTG melt production is confined to low pressures, with a temperature gradient mainly controlled by the temperature of the intrusions. During the dripping stage, the thickness of the proto-mafic crust rapidly increases, shifting the melting conditions of the mafic protolith to higher pressures and temperatures, crossing the P–T conditions necessary for producing TTG magmas with Archean major and trace element compositions shown by Palin et al. (2016a). Our reference scenario features high-pressure melting conditions at the end of the dripping stage. However, the variability of the melt conditions and their median values depends strongly on the initial conditions (e.g. high T_{Moho} produce a horizontal homogenous thickened crust, which limits high pressure TTGs). The ratio between mafic intrusion/extrusion exerts a strong control and increasing it would result in a thinner crust that is completely outside the optimum field of TTGs generation. However, a slight increase (e.g. 65%) produces a perfect fit to the TTGs' optimum field with respect to the reference scenario (see Supplementary Material, Fig. A10-A11, A13). TTGs have been classified in three categories: low pressure (LP, $0 < P < 1.0$ GPa), middle pressure (MP, $1.0 < P < 2.0$ GPa) and high pressure (HP, P>2.0 GPa) (Moyen, 2011; Fischer and Gerya, 2016a). The classification is based on a global dataset of TTGs, and on the extensive experimental studies on TTGs generation (Moyen and Stevens, 2006). The three categories represents three different P-T conditions in which TTGs might have been generated, in which the most important parameter is the pressure of generation. Such classification has been used to infer three different geodynamic settings to account TTGs production. The most abundant category is represented by the MP TTGs, 60% of all TTGs analyzed, while the other two represents respectively 20% of the total TTGs analyzed (Moyen, 2011). The relative amount of these three type of TTGs have been widely used in geodynamical modeling to assess the proper condition of the TTGs generation (Rozel et al., 2017; Fischer and Gerya, 2016a). Yet, the validity of this classification has been recently questioned using thermodynamic modeling (Palin et al., 2016a), which demonstrate that the three types can be generated by prograde metamorphic paths over a much narrower pressure window. Our numerical experiments agree with Palin et al. (2016a), however, if they are compared with the Moyen (2011)'s classification, our model mostly are unable to replicate the distribution of the three categories. However, the model that most closely fits Moyen (2011)'s classification is the one featuring the lowest I_R (i.e. 20% see Figure S13). If I_R evolves during the whole experiments and accordingly the rheology of the crust, it is possible to cover the full gamut of conditions predicted by Palin et al. (2016a) and Moyen (2011).

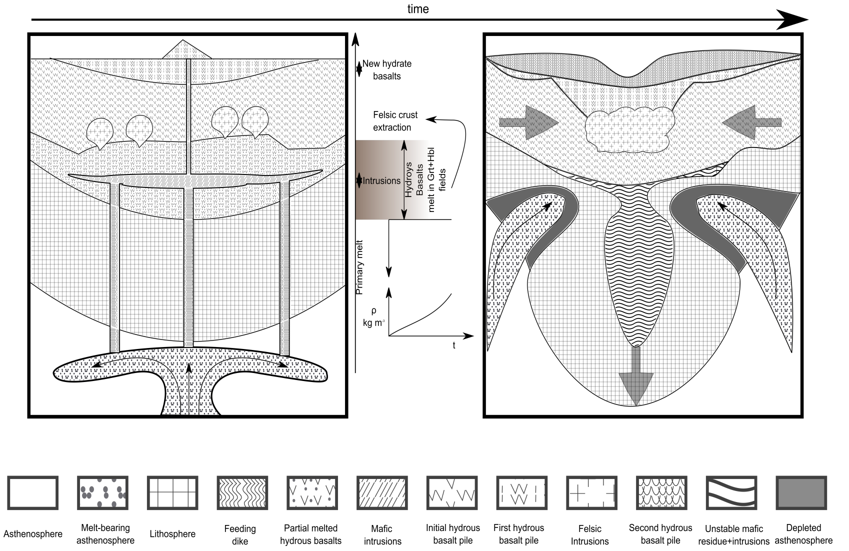

Figure 7: **Simplified cartoon model** : Melt coming from the astenosphere percolates through the lithosphere, heating and both plastically and thermally weakening it. Part of the mafic melts are emplaced in the lower crust, while the remnants are erupted. The thickness of the crust increases, while the thermal energy provided by the intrusions starts heating the previously generated hydrous crust which melts producing large amounts of garnet enriched residuum. As soon as a critical amount of residuum is reached, RTIs are triggered, and asthenosphere fills the space left by the delaminated lithosphere. This results in a feedback between mantle melting and new crust production that enhances convection yielding a colder and depleted mantle.

3 Discussion

The thermal–tectonic effects of partial melting of an Archean mafic crust have been incorporated into two-dimensional numerical simulations of early-Earth geodynamics, and show that drip tectonics can occur at even lower T_P than previously thought, owing to the concurrent emplacement of intrusions and production of garnet-rich mafic residuum via melting and melt loss. In our experimental framework, the mantle magmatic processes mostly control the rheological and density structure of the crust by heating it and producing felsic melts and complementary mafic dense residuum. Therefore, T_P control is indirectly exerted through the production of mafic magmas that fuel the process of continental crust production leading ultimately to RTIs. A colder T_P (<1550°C) reduces the magmatic flux coming from the mantle, increasing the timescales of the incubation stage and increasing the importance of the mafic residuum on the dynamics of the experiment (see Fig. 7 for a brief summary). Without the production of mafic dense residuum, the RTIs would not spontaneously form at this reduced T_P (Johnson et al., 2013) .

The large-scale geodynamic processes observed in our numerical experiments involving melting and foundering of the residue can be compared in some respects to those proposed for oceanic-arcs (Jagoutz and Kelemen, 2015; Jagoutz, 2014), where the production of felsic crust via crystal fractionation of hydrated mafic parental magmas produces dense mafic cumulates. Both processes have similar consequences: the ultramafic cumulates and the residuum of the fractional crystallization founder back into the mantle leaving a crust enriched in felsic material (Behn et al., 2007). The operation of RTIs at present-day T_P highlights how they are an inevitable consequence of continental crust production and mantle magmatic processes. In the modern Earth, the mantle is partially molten in spatially restricted domains. Oceanic arcs are magmatically active as the subducting slab release fluids into the mantle triggering massive melting and reducing its viscosity (Schmidt and Poli, 1998; Behn et al., 2007), which jointly with the differentiation of mafic melts favours RTIs. However, this process would not trigger the feedback that induce a high felsic crust production and is different from drip-vertical tectonics (Fischer and Gerya, 2016a; Zegers and van Keken, 2001; Bédard, 2006). Our results predict that RTIs could have driven the generation of continental crust for the whole Archean, providing further support to the suggestion that has been made in previous numerical studies (Fischer and Gerya, 2016b; Sizova et al., 2015), and that dripping is associated with a rapid decrease of T_P. Lourenço et al. (2018) observed the same behavior in global scale geodynamical models, and emphasized the role radiogenic heating has on the thermal history of rocky planets. Our results show that high mantle potential temperature could not last for long geological timescales, and that the radiogenic heat affects the long term stability of the lithosphere regardless of the initial T_P.

4 Conclusions

Whilst a widely used estimate of Meso-Archaean mantle T_P of ~ 1600°C has been proposed based on calculated primary magma solutions for a small number of non-arc basalts (Herzberg et al., 2010), a more recent analysis of a significantly larger dataset (22,000 samples) suggests that the Archean mantle may have had a lower T_P value of ~ 1500°C (Ganne and Feng, 2017). Our models show that large volumes of TTGs can be produced via crustal melting without requiring exceptionally high T_P, and thus provide further support to the lowermost T_P estimates. Several studies argue that the average upper-mantle T_P could have been lower than the current estimation and invoke local temperature anomalies being responsible for rocks recording apparent high T_P (Ganne and Feng, 2017; Arndt, 2013; Kamber, 2015). However, metamorphic activity during the Archean seems to have been frequently punctuated by magmatic events, correlating with enhanced amounts of continental crust production, suggesting even fluctuations as function of the time (Bédard, 2018; Moyen and Van Hunen, 2012; O'Neill et al., 2015). These findings prompt the idea that regardless of the inherent variation of T_P , the thermal history of the Earth has not been monotonic (O'Neill et al., 2015; Sleep, 2000; Davies, 1995; Condie et al., 2018). It has been argued that such peak corresponds to plate tectonic activity to justify the production of continental crust (Moyen and Van Hunen, 2012; O'Neill et al., 2015), while our simulations demonstrate that dripping assisted continental crust production could be a viable alternative, consistent with the geological record. Therefore, variation of T_P either in space and time can potentially trigger this process while creating large amounts of felsic crust. The only requirement is that the whole upper mantle is sufficiently hot to produce mafic melts or that the crust bears sufficient amount of dense mafic residuum and intrusions (e.g. $T_P \geqslant$ 1450–1500 °C). The Archean upper mantle could therefore not have featured a consistent T_P everywhere, supporting suggestions made from various independent lines of evidence for intermittent thermal histories on the early Earth in which fluctuations of T_P were associated explicitly with periodic mantle overturn (Davies, 1995; Condie et al., 2018) and with local variation of T_P associated with long lasting plumes in a stagnant lid planet (Bédard, 2018).

Introduction This supplementary contains additional pictures that assist the main manuscript, supporting tables and information concerning the initial setup, experimental designs and the technical information of the hardware used to perform the simulation.

1. Initial Setup
We use a regional scale numerical domain (1000 x 660 km along x and z direction). We employ the same number of grid nodes in both direction (331 x 331 nodes, which yields a resolution of 3000 x 2000 meters along x and z direction). We employ LBB stable Q_2P_{-1} elements. The mechanical boundary conditions are free surface at the top (Kaus et al., 2010), and free slip for the right, left and bottom boundary. Temperature has isothermal boundary conditions at the top and bottom (20 °C at the top, the bottom boundary conditions depends on the initial mantle potential temperature, T_P), meanwhile the left and right boundary condition are no flux boundary conditions. The initial compositional field is made of two main layers: lithosphere and asthenosphere mantle. The asthenosphere mantle was modelled as fertile peridotite (MFP) with dry olivine rheology or wet olivine rheology (Hirth and Kohlstedt, 2004) and it extends from the base of lithosphere to the bottom of the numerical model. It represents the source reservoir for the EAT basalts and chemically evolves accordingly the petrological model employed. The initial lithosphere is composed of two layers: lithospheric mantle and the crust. The crust is always 1/3 of the total lithosphere thickness, which is 80 km for the reference test (i.e. 24 km crust thickness). The crust is made of two layers: upper crust (upper 2/3) and lower crust (lower 1/3 of the total thickness (i.e. 8 km, for the reference model). The upper crust is modeled as hydrated enriched basalt (BS1) with a wet quartzite rheological flow law (Ranalli, 1995) meanwhile the lower crust is modelled as intrusive layer with BS4 phase diagrams and with mafic granulite rheology (Ranalli, 1995). Lithospheric mantle is modelled with the MDS1 and it has always dry olivine rheology (which can be modified to simulate stiffening adjusting the pre-exponential factor value). The initial geotherm is double stage and is fully characterized by the T_P (°C), adiabatic gradient (0.4 °C/Km) and Moho temperature, T_{Moho} (°C). The top boundary is always °C, and the bottom boundary is computed accordingly to the initial mantle potential temperature and adiabatic gradient (e.g. for the reference test is 1814 °C). The Moho temperature varies accordingly the numerical experiments (it ranges from 800 to 1200 °C).
Our systematic analysis tested the role of the differentiation on the geodynamic of the upper mantle. We track several properties: the crust composition, the mantle potential temperature and the relative time-scale of the processes. The crust composition, F, is defined as the relative amount of felsic crust composition respect to the vertical direction:

$$F = \left(\frac{Felsic}{Mafic + Felsic}\right) * 100 \tag{A1}$$

The produced compositional profiles are used to compute the average composition and its standard deviation. As a complementary parameter, we track the conversion factor, which represents the amount of BS1 converted into the other three stages:

$$C = \left(1 - \frac{BS1}{BS1 + BS2 + BS3 + BS4}\right) * 100 \tag{A2}$$

We tested a wide range of parameters ranging from the Moho temperature, rheology, initial thickness and mantle potential temperature and melt extraction parameters producing several sets of experiments. The duration of the dripping stage is derived using T_P vs Time curves, taking the time before the mantle potential temperature drop and the time associated with the minimum T_P. Every T_P vs time curve in the simulations show a slight increase in T_P during the initial stage, a drop of mantle potential temperature and then a slow increase of mantle potential temperature. This approach gives us the opportunity to compare several numerical experiments whose timescale is different, allowing comparison of compositional patterns (F or C) at the beginning or end of the dripping stage.

2. Experimental Systematic and Hardware informations

We organize the experiments following different systematics, in which we tested several parameters against each other starting from the reference test. Such approach elucidate the complex interaction between the parameter. S1-S2, which explore the relative effects of the T_{Moho}, ϕ_{dry}, λ_{melt} and mantle rheology; S3, which explore the effect of the amount of intrusion respect the extrusion, and the efficiency of melt extraction (represented by M2); S4 exploring the effect of mantle potential temperature and initial thickness (see Table S2, for further details). All the experiments have been performed using *MVEP2*, an open source MATLAB〃 code (R2016b) (https://bitbucket.org/bkaus/mvep2). The numerical experiments were performed using GAIA (*4x6276 AMD Interlagos, 16 cores,2.30 GHz,12MB, 12 MB Cache, 512 GB RAM*) and IRIS (*4xE5-4640 Intel Xeon 8 cores CPU, 2.54 GHz,16 MB cache, 512 GB RAM*) at the Institutes of Geosciences, JGU Mainz, Germany. Each simulation takes 4-6 weeks and they were interrupted during the “static stage”, when the mantle potential temperature and the low amount of fertile mantle prevents further development.

3. Supporting Figures and Tables

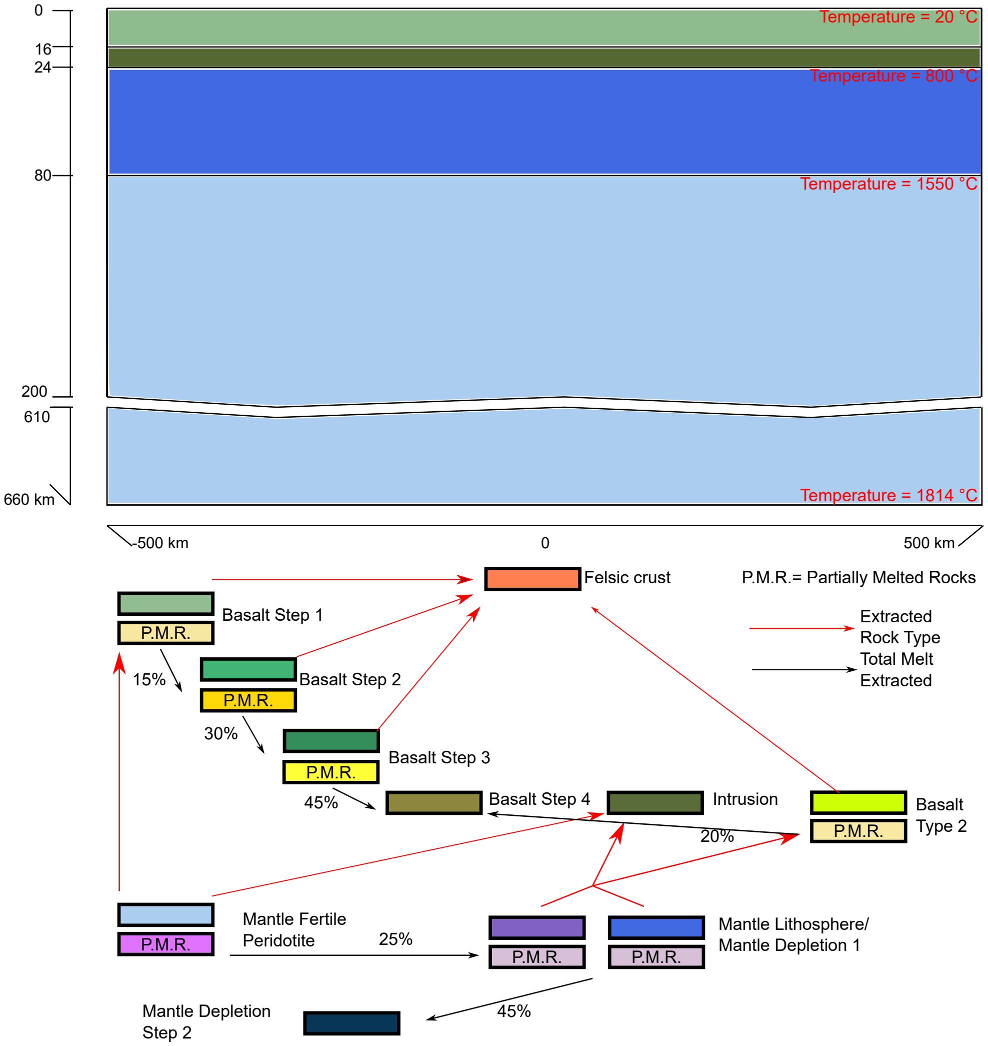

Figure A1: **Initial Setup**: Each extraction events from the mantle produce extrusion and intrusion (Basaltic Step 1 and Intrusion). Red arrows connect the sources with the extracted rock type. Mantle Fertile peridotite produces Basalt Step1 and dry intrusion. Black arrow connects the successive Step of depletion. If a particle associated with Basalt Step 1 reaches 15 % of total melt extracted, its phase diagram and rock type is changed into Basalt Step 2.

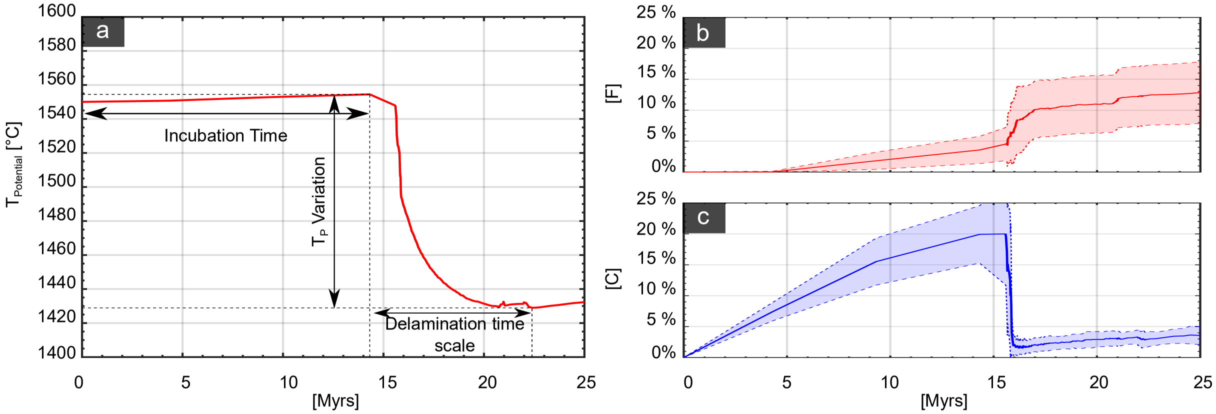

Figure A2: **Complementary Information Figure 1: a):** Temporal evolution of mantle potential temperature; **b):** Average amount of felsic material in the crust (F) (see eq. A1) versus time. The thick line represents the effective average, while the red shaded area between the dashed lines are the standard deviation of the data. Drip formation results in a rapid increase in felsic crust; **c):** Average C against time, where C represents the amount of converted basalt stage 1 (see equation 1.19). When the drip stage starts, C suddenly drops, implying a total foundering of the dense residuum into the mantle, and allowing a steady state consumption of the mafic crust during the static stage. The thick line represents the effective average, while the blue shaded area between the dashed lines are the standard deviation of the data.

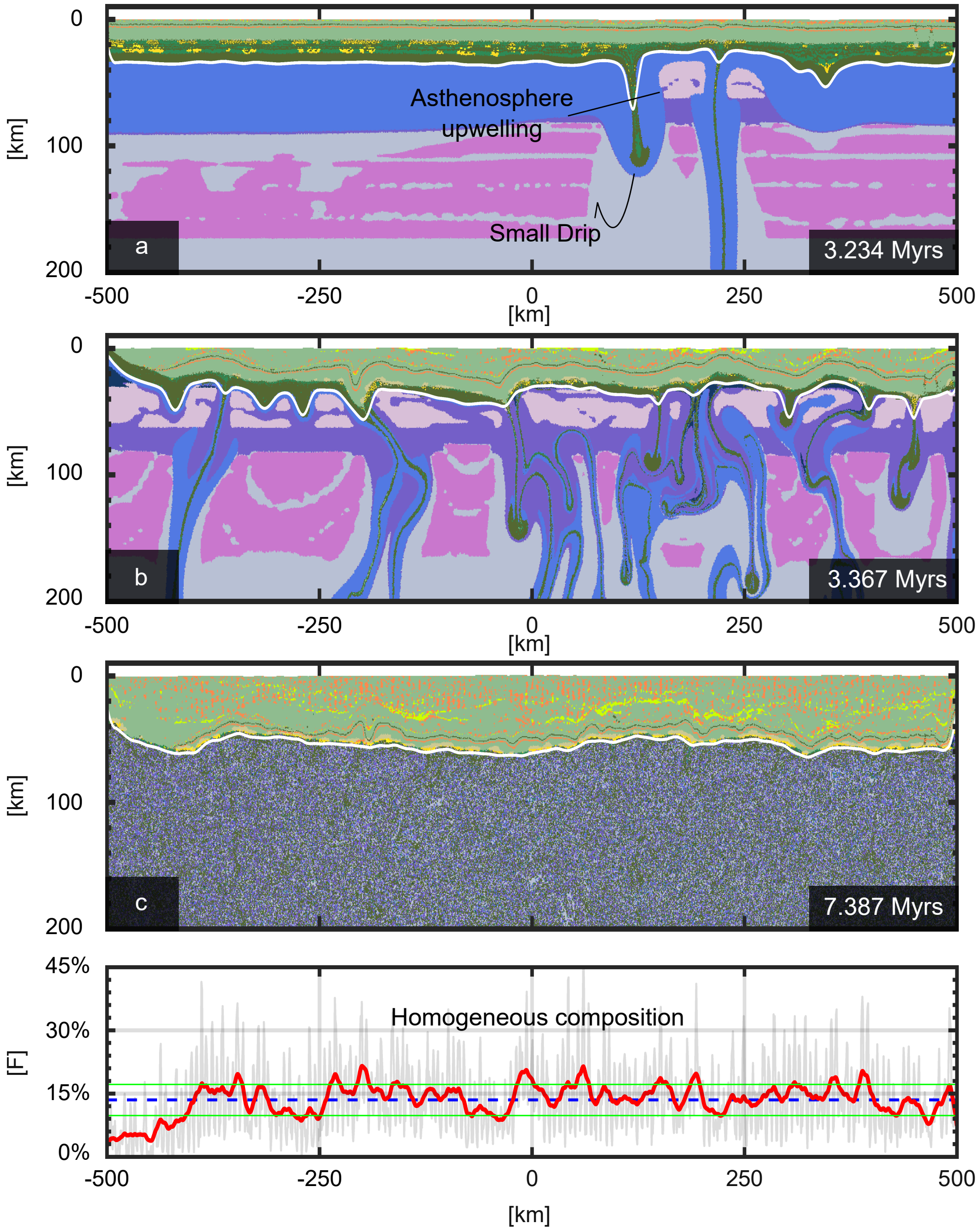

Figure A3: **Effect of high T$_{Moho}$(λ_{melt} = 0.01, ϕ_{dry}=30°):** The initial Moho temperature is 1200 °C. **a):** Incubation stage; **b):** Dripping and Magmatic thickening stage; **c):** Static stage and compositional profile along the x direction (see S2 for further details)

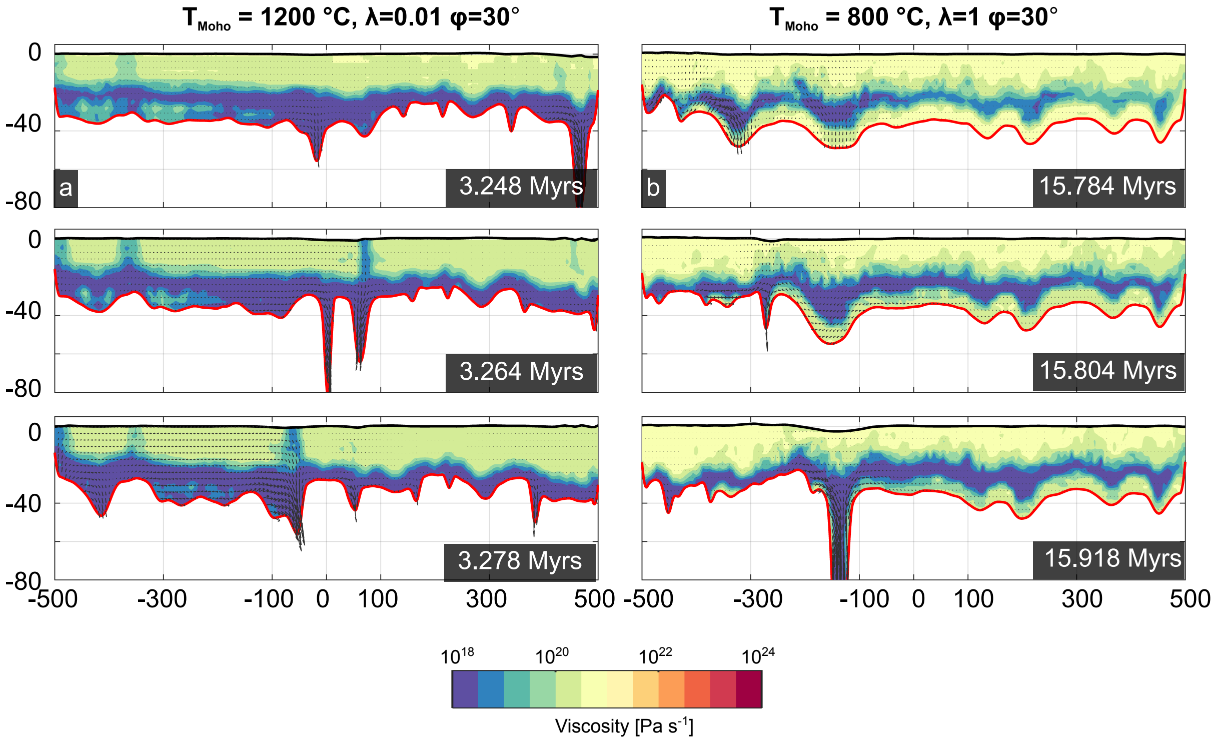

Figure A4: **Effect of high T_{Moho} = 1200 °C and λ_{melt}=1 on the drips: a):** The initial T_{Moho} is 1200 °C, while the other parameters have been kept the same respect to the reference test. During the onset of the dripping stage, the higher temperature jointly with the production of dense residuum, trigger the RTIs instabilities. Owing to the higher temperature, the dense residuum/intrusion are decoupled from the upper crust. Albeit the upper crust is deformed, is not experiencing significant deformation events; **b):** The melt weakening factor is not active. During the dripping stage the dense material transmit stress, but the crust is strong, and it is not yielding. This entails that the plastic deformation plays a fundamental role in the intraplate deformation stage and controls the ability of the crust to transfer pristine, hydrated/felsic material to the mantle.

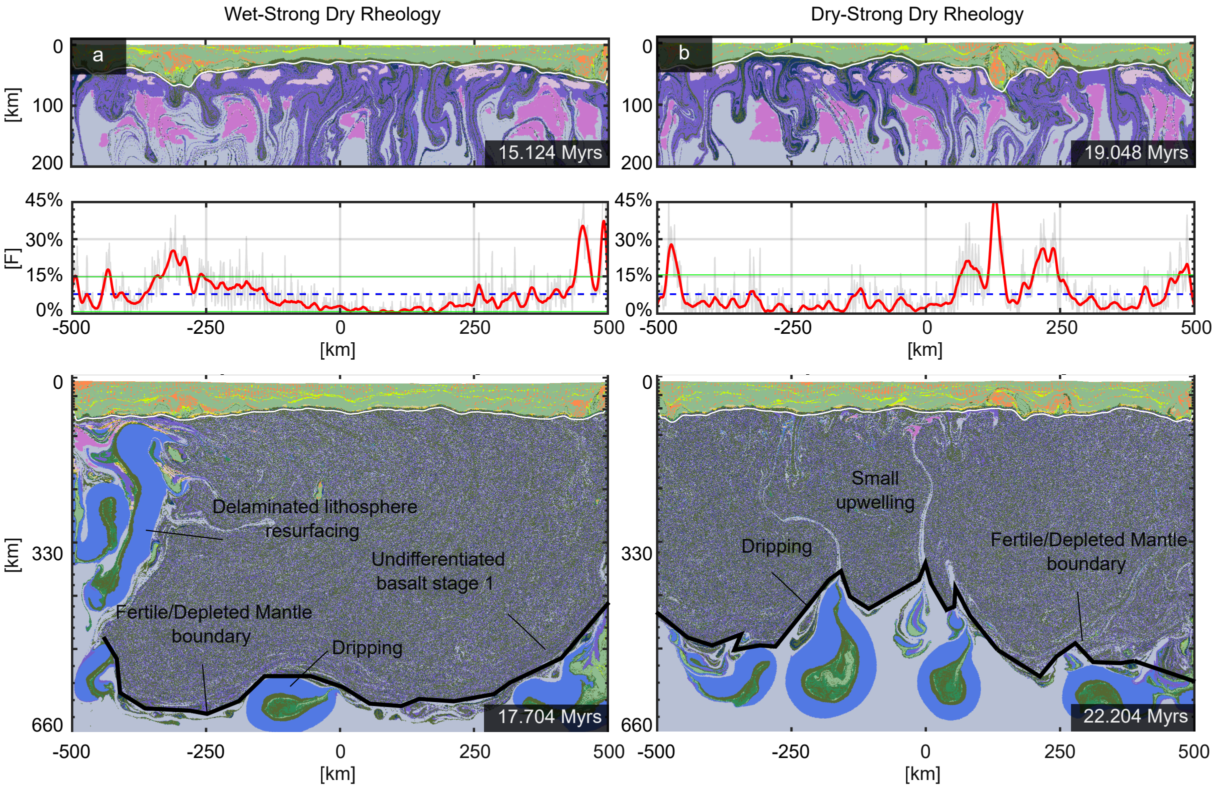

Figure A5: **Effect of the mantle depletion stiffening: a):** Experiment in which the mantle starts from a wet rheology and evolves towards a strong dry olivine rheology. To increase the effective viscous strength of the material, the pre-exponential factor of either the diffusion and dislocation creep has been incremented by one order of magnitude. The first picture in the upper left represents the lithospheric scale view of the tectonic thickening stage together with the compositional plot. The bottom left picture depicts the whole numerical domain during the static stage. The shape of the initial drip spans from tear shape to planar. Most of the mantle has been converted into the second step of depletion, and the mafic and ultramafic residuum are well mixed with the mantle. Only small fraction of primitive mantle has been preserved during the drip stages; **b):** Experiment in which the mantle starts from the dry olivine rheology then it evolves towards the strong dry rheology. The timescales of the processes increase, and most of the initial drip has a tear shape. The amount of converted mantle is less than the left experiments.

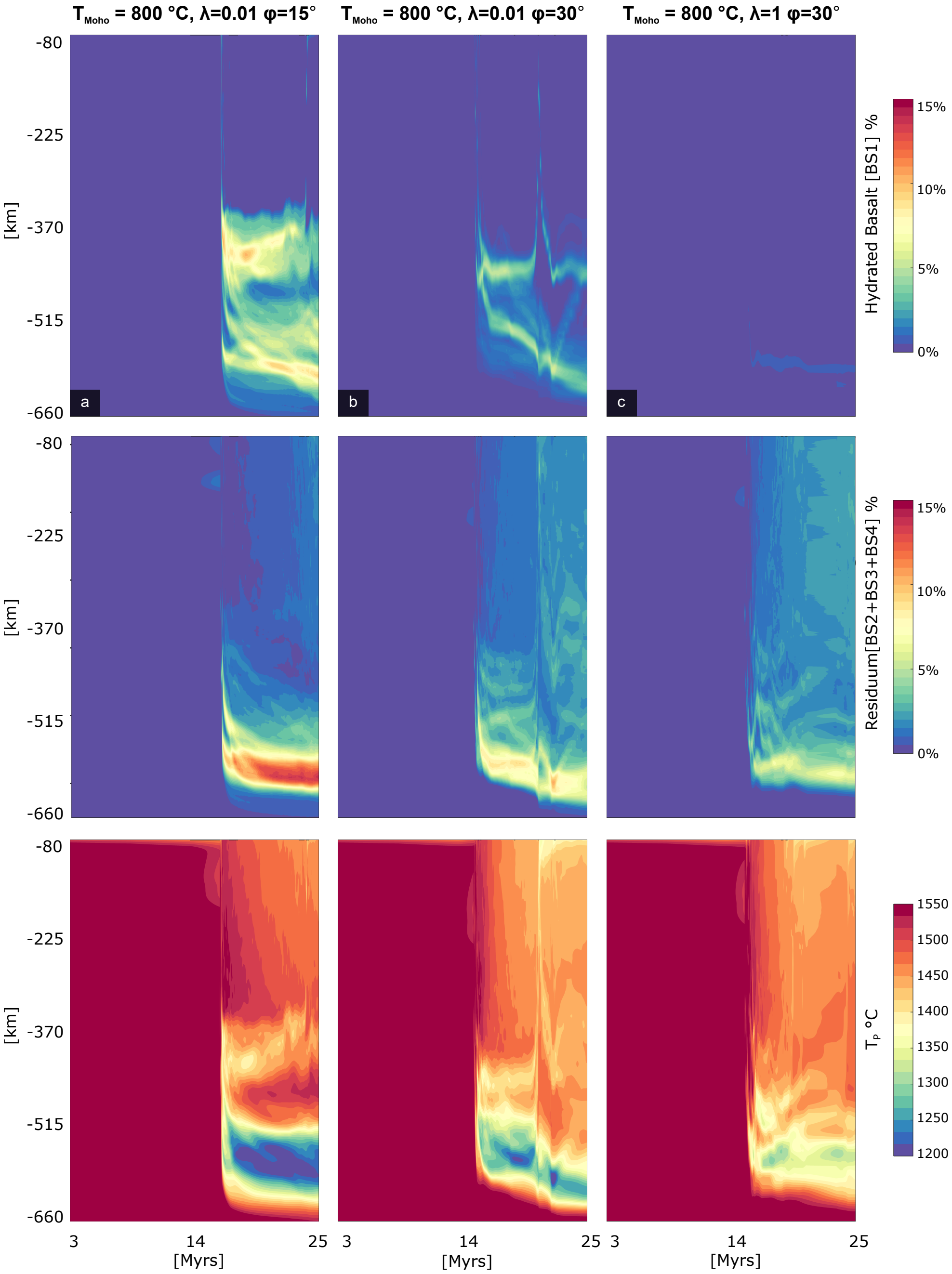

Figure A6: **Mantle thermal-compositional evolution:** Each column represents the data associated with a numerical experiment, while each row represents the different composition profile. The first row is the hydrous basalts that foundered into the mantle, the second row the amount of residuum and the third one the mantle potential temperature. Each plot represents the evolution of the horizontal average composition/temperature against time and depth. The dripping stage mix the mantle, but it may create compositional-thermal heterogeneities. The development of thermal-compositional heterogeneities is function of the mobility of the crust, and its ability to plastically yield.

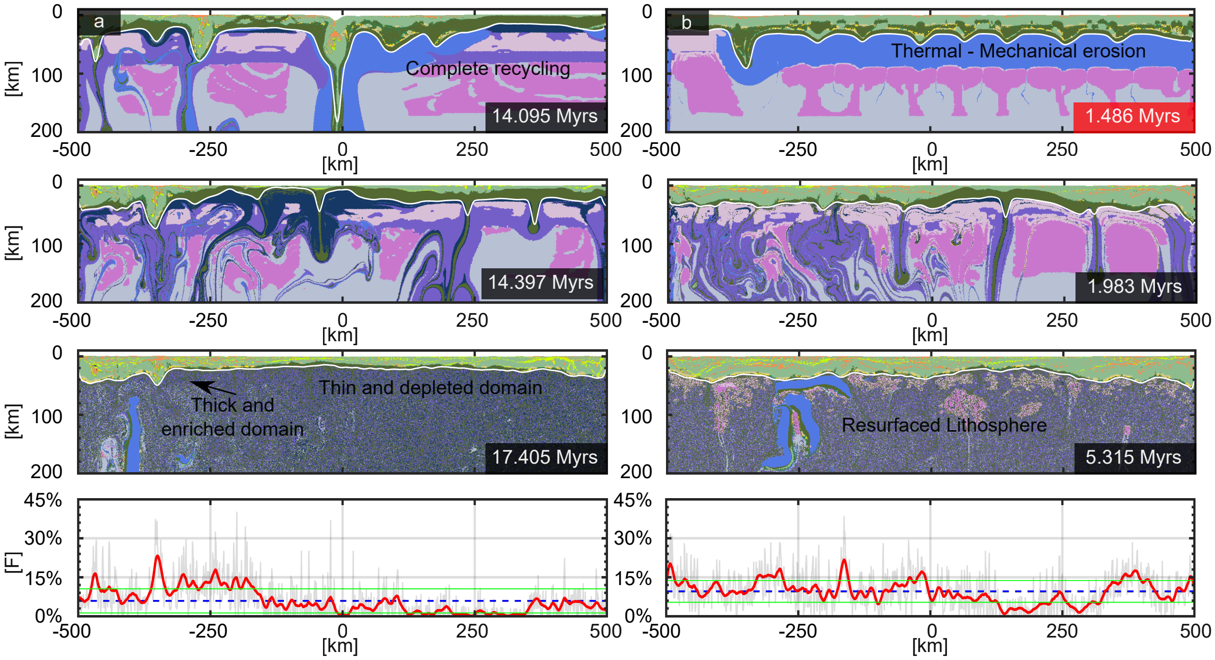

Figure A7: **Effects of the relative amount of intrusion per each extraction event and of the melt left after melt extraction event: a):** Experiment that has higher amount of intrusion per each extraction events. 80% of the total extracted melt from a mantle source (MDF or MDS1 and Lithospheric Mantle) is converted into dense mafic intrusions. The melt that remains on the source is the same of the reference test (0.2%). The first-middle left pictures represent the drip stage in which most of the older crust is recycled into the mantle. The third and the bottom left represent the static stage and the relative compositional profile; **b):** Experiments that has the same data of the left ones. The amount of melt that has to be left in the source is increased (2%). In such condition the drips are promoted since the beginning of the numerical experiments, achieving the static stage in less than 5 Myrs. The final thickness increases and the compositional difference between depleted and enriched domain are less pronounced.

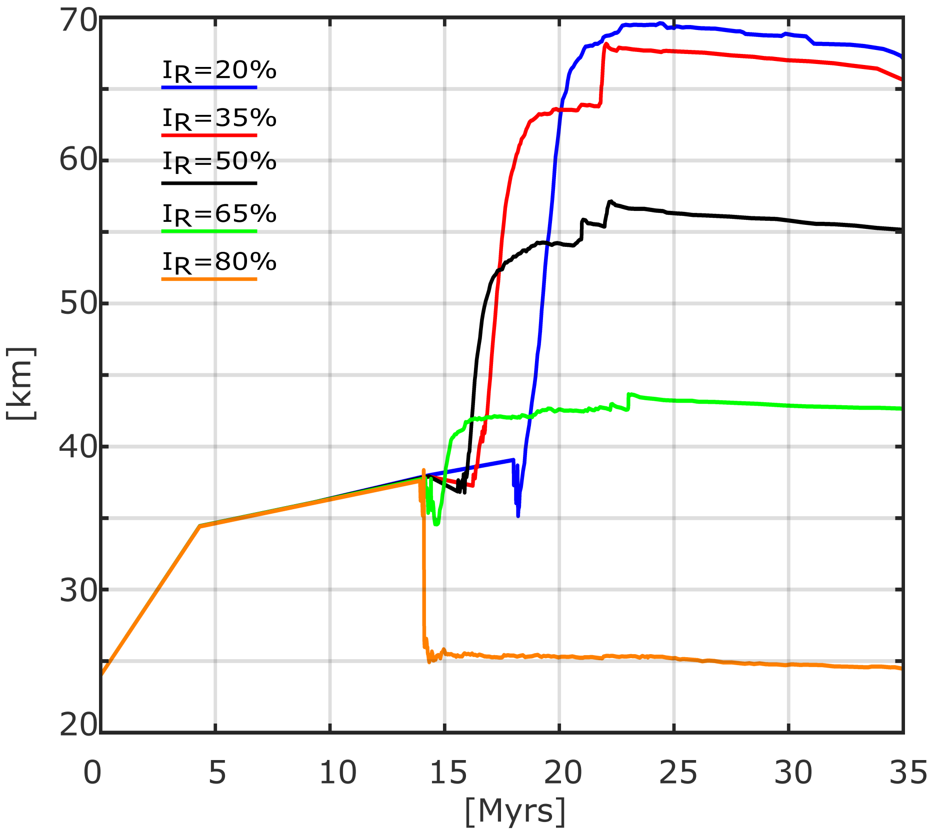

Figure A8: **Average crustal thickness against time for different I_R values;**

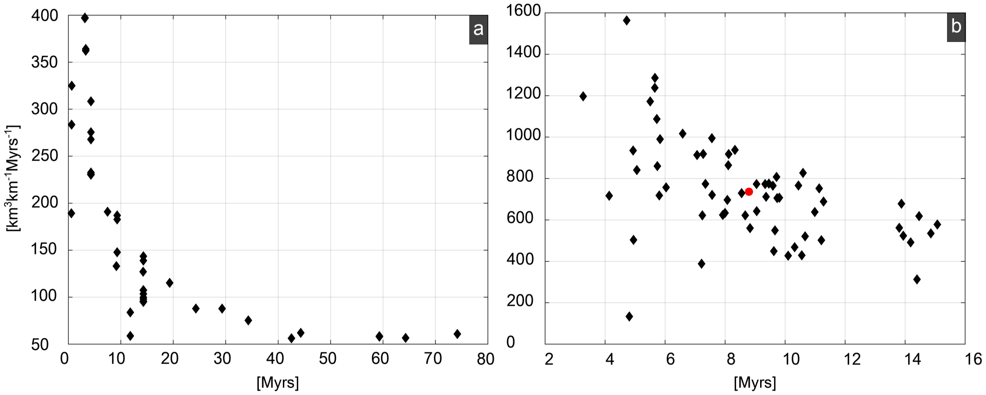

Figure A9: **Crustal production: a):** The continental crust production during the incubation stage vs the duration of this stage; **b):** The continental crust production during the dripping stage vs the duration of the dripping stage. The red dot represents the average crust production of the all experiments.

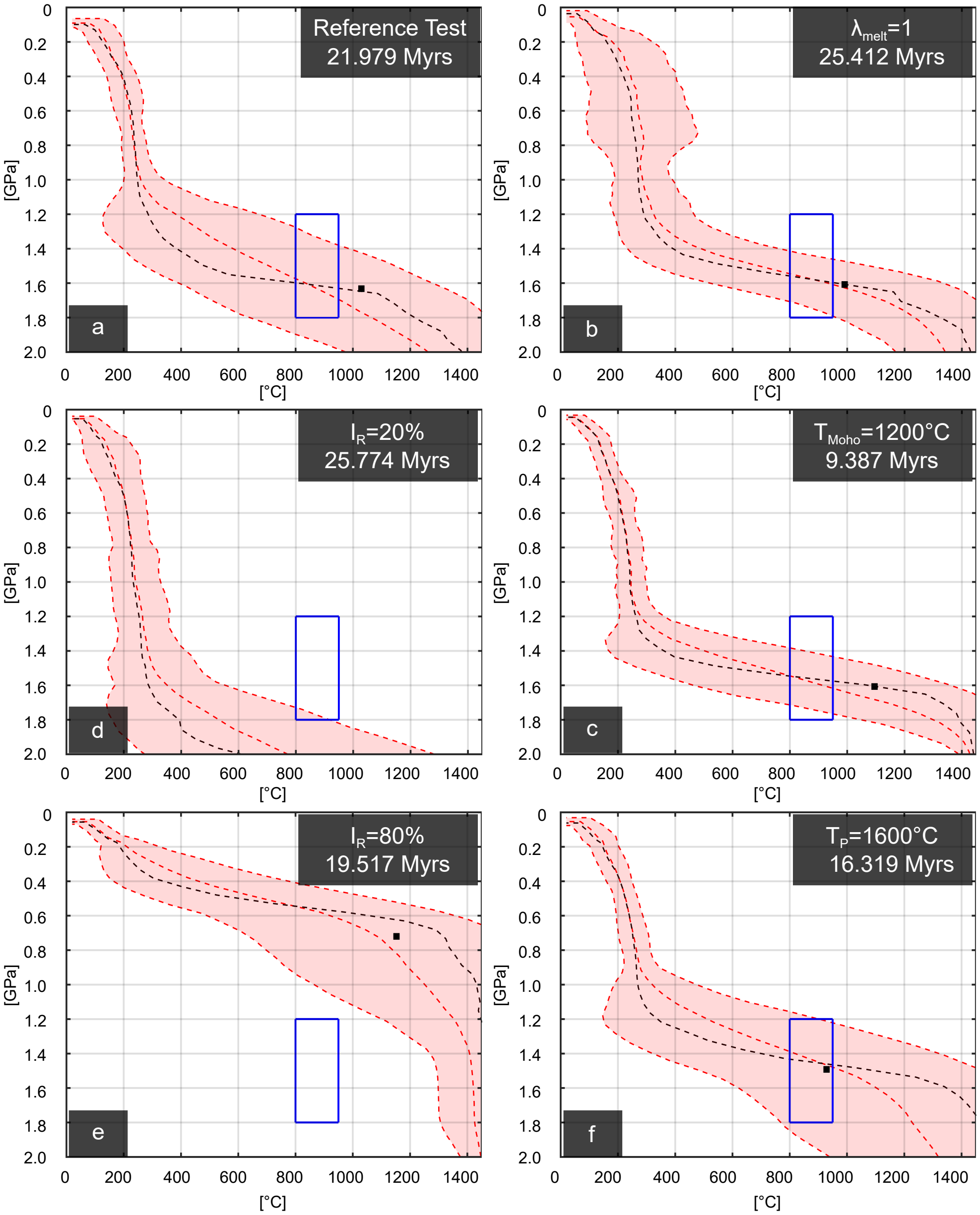

Figure A10: **Geothermal gradient achieved after the drip stage :**Each figure represents the variability and average P–T conditions of the crust. The dashed lines represent the upper and lower standard deviation. The median and average P–T conditions are compute averaging the conditions along x direction. The red dashed line in the middle of the interval represents the average. The black line is the median of the P–T conditions taken. The black square represents the average P–T conditions of the Moho. The blue square box represents the set of optimum conditions to generate TTG trace element signature. All the profiles are taken after the dripping stage when the average velocity at Moho depth reaches the steady state. Each subfigure represents one experiment, in the upper right corner are indicated the parameter that have been chanced respect to the reference test, and the timing at which such profile has been computed.

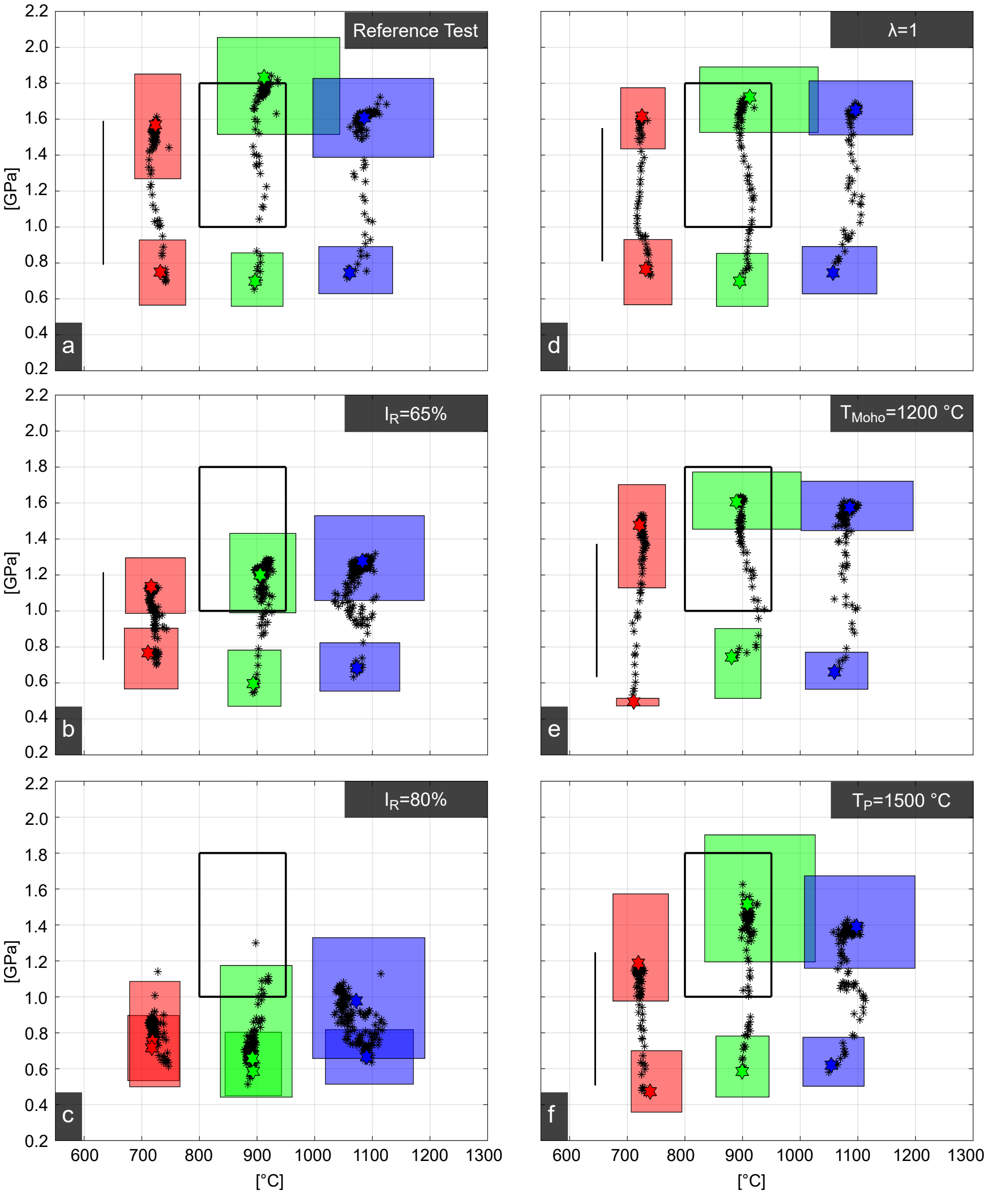

Figure A11: **Melting condition for each basalt step:** The colored boxes represent the average conditions of melting during the incubation stage and at the end of the dripping stage for each Basalt Step (BS1-3). Red is related to BS1, while green and blue are respectively BS2 and BS3. The hexagonal stars are the median condition, while the black asterisk that connect the incubation stage with the end of the dripping stage represent the median melting condition experienced during the whole dripping stage. Each picture represents a different experiment. In the upper right corner are indicated the input parameter that have been changed respect the reference test.

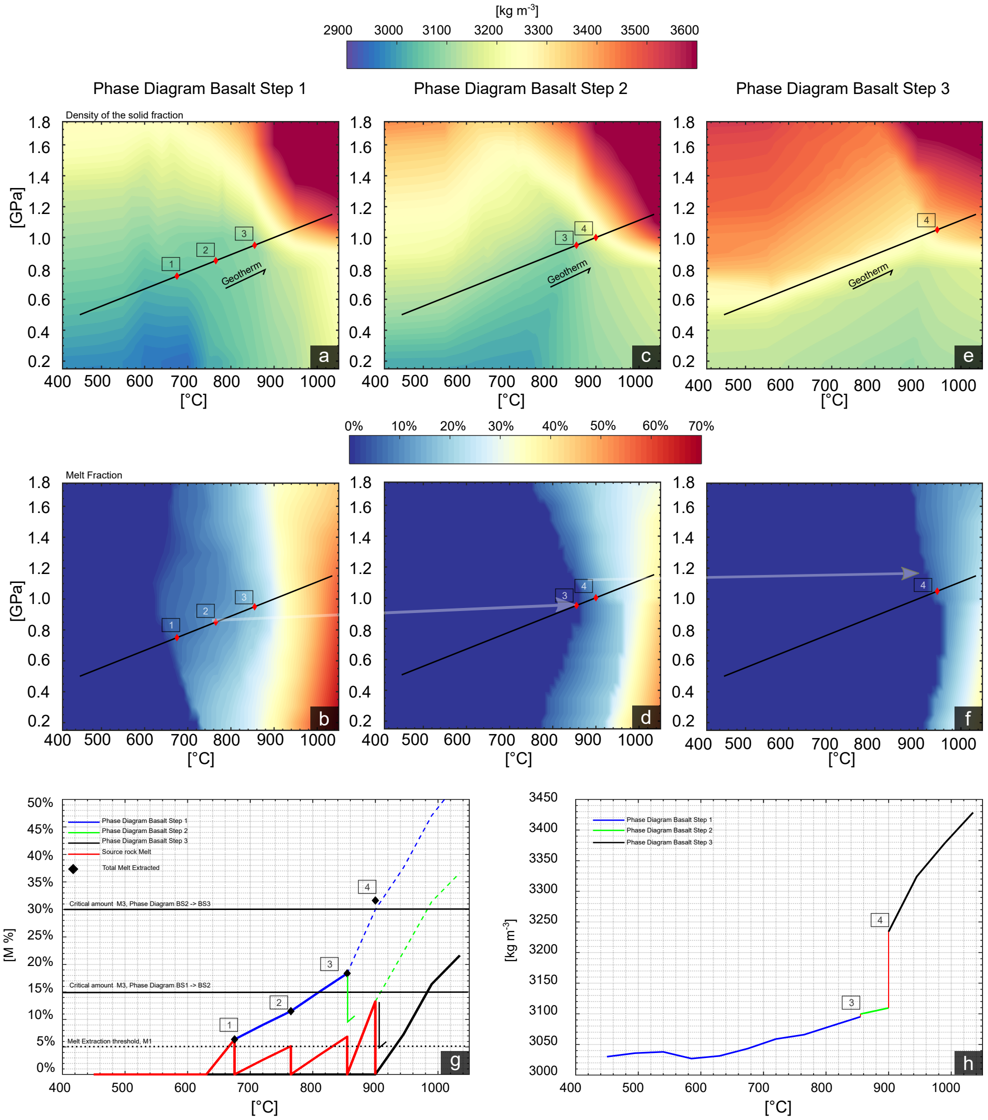

Figure A12: **Melt extraction: a-c-e):** Represents the density field associated with BS1,BS2 and BS3 respectively. The thick black line represents a hypothetical geotherm of 900°C/GPa. The diamond point represents extraction events that have been performed assuming a threshold of 5%; **b-d-f):** Represents the relative volumetric amount of melt. At the top of the field is plotted the geotherm and the relative extractions events; **g):** 1D representation of melt extraction processes. The red thick line represents the effective amount of melt stored in the particles. Melt extraction is allowed if the melt is exceeding 5% (dashed line). Once it exceeds it in the point 1, the melt is taken away from the source, and it remains dry. Then the system starts accumulating again melt. The effective amount of melt is interpolated from the phase diagram BS1 (blue line) then corrected with the total melt extracted within this melting step. The process is repeated other two times, until the total melt extracted (diamonds) exceed 15% threshold. After the third extraction the phase diagrams is changed, and the melt accumulation is ruled by the second phase diagrams (green line). We assume that the increase of temperature is fast, so once it reaches the 4 extraction events the total melt extracted is equal to the final threshold, and then the density and the melt quantity is interpolated from the third phase diagrams; **h):** Represents the density evolution experience by the marker as function of the P-T condition, and as function of the depletion. The last step of melt extraction occurs in the garnet tie line, entailing a significant jump of the density of the system.

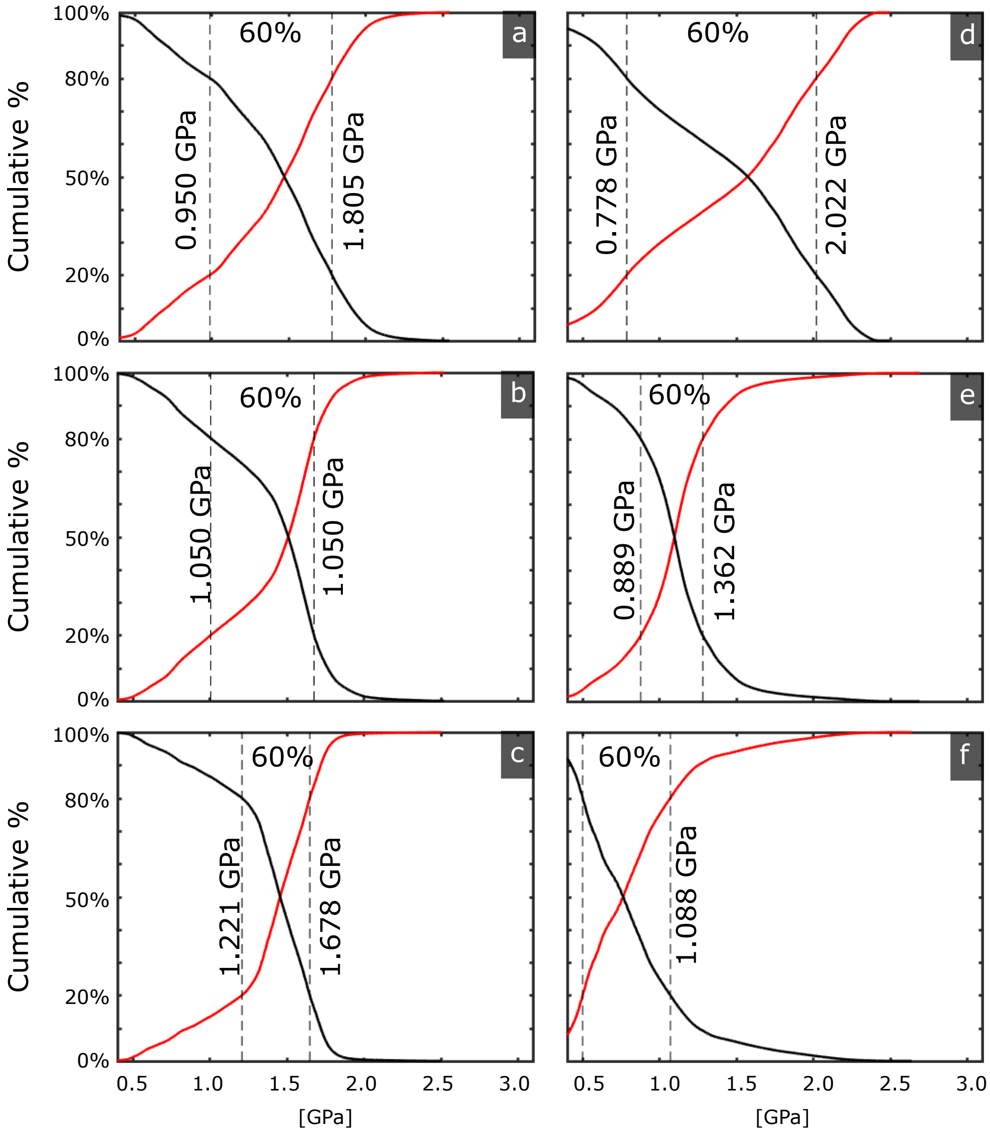

Figure A13: **Distribution of the melting pressures of the all basalt types:** We produce a cumulative distribution of the pressure condition at which any of the basalt types are melting. We plot the cumulative distribution(red thick line) and the reverse cumulative distribution (black thick line). All the experiments have the same condition of the reference test (panel **a)**) except for: **b):** T_{Moho}=1000 $^{\circ}C$; **c):** T_{Moho}=1200; **d):** I_R=20%; **e):** I_R=65%; **f):** I_R=80%.

References

Anhaeusser, C.R., 2014. Archaean greenstone belts and associated granitic rocks–a review. Journal of African Earth Sciences 100, 684–732.

Arndt, N.T., 2013. The formation and evolution of the continental crust. Geochemical Perspectives 2, 405.

Beall, A.P., Moresi, L., Stern, T., 2017. Dripping or delamination? a range of mechanisms for removing the lower crust or lithosphere. Geophysical Journal International 210, 671–692.

Bédard, J.H., 2006. A catalytic delamination-driven model for coupled genesis of Archaean crust and sub-continental lithospheric mantle. Geochimica et Cosmochimica Acta 70, 1188–1214.

Bédard, J.H., 2018. Stagnant lids and mantle overturns: implications for archaean tectonics, magmagenesis, crustal growth, mantle evolution, and the start of plate tectonics. Geoscience Frontiers 9, 19–49.

Bédard, J.H., Brouillette, P., Madore, L., Berclaz, A., 2003. Archaean cratonization and deformation in the northern superior province, canada: an evaluation of plate tectonic versus vertical tectonic models. Precambrian Research 127, 61–87.

Bédard, J.H., Harris, L.B., 2014. Neoarchean disaggregation and reassembly of the superior craton. Geology 42, 951–954.

Bédard, J.H., Harris, L.B., Thurston, P.C., 2013. The hunting of the snArc. Precambrian Research 229, 20–48. URL: `http://dx.doi.org/10.1016/j.precamres.2012.04.001`, doi:10.1016/j.precamres.2012.04.001.

Behn, M.D., Hirth, G., Kelemen, P.B., 2007. Trench-parallel anisotropy produced by foundering of arc lower crust. Science 317, 108–111.

Bodorkos, S., Sandiford, M., Benn, K., Mareschal, J., Condie, K., 2006. Thermal and mechanical controls on the evolution of archean crustal deformation: examples from western australia. GEOPHYSICAL MONOGRAPH-AMERICAN GEOPHYSICAL UNION 164, 131.

Bouhallier, H., Chardon, D., Choukroune, P., 1995. Strain patterns in Archaean dome-and-basin structures: The Dharwar craton (Karnataka, South India). Earth and Planetary Science Letters 135, 57–75. doi:https://doi.org/10.1016/0012-821X(95)00144-2.

Brown, M., 2007. Metamorphic Conditions in Orogenic Belts: A Record of Secular Change. International Geology Review 49, 193–234. URL: `https://doi.org/10.2747/0020-6814.49.3.193`, doi:10.2747/0020-6814.49.3.193.

Brown, M., Johnson, T., 2018. Secular change in metamorphism and the onset of global plate tectonics. American Mineralogist 103, 181–196.

Cawood, P.A., Hawkesworth, C., Dhuime, B., 2013. The continental record and the generation of continental crust. Bulletin 125, 14–32.

Chardon, D., Choukroune, P., Jayananda, M., 1996. Strain patterns, décollement and incipient sagducted greenstone terrains in the archaean dharwar craton (south india). Journal of Structural Geology 18, 991–1004.

Chardon, D., Choukroune, P., Jayananda, M., 1998. Sinking of the dharwar basin (south india): implications for archaean tectonics. Precambrian Research 91, 15–39.

Choukroune, P., Bouhallier, H., Arndt, N., 1995. Soft lithosphere during periods of archaean crustal growth or crustal reworking. Geological Society, London, Special Publications 95, 67–86.

Clauser, C., Huenges, E., 1995. Thermal conductivity of rocks and minerals. Rock physics & phase relations 3, 105–126.

Collins, W., Kranendonk, V., MJ, Teyssier, C., 1998. Partial convective overturn of archaean crust in the east pilbara craton, western australia: driving mechanisms and tectonic implications. Journal of Structural Geology 20, 1405–1424.

Condie, K.C., 2003. Incompatible element ratios in oceanic basalts and komatiites: tracking deep mantle sources and continental growth rates with time. Geochemistry, Geophysics, Geosystems 4, 1–28.

Condie, K.C., 2005. High field strength element ratios in archean basalts: a window to evolving sources of mantle plumes? Lithos 79, 491–504.

Condie, K.C., Aster, R.C., van Hunen, J., 2016. A great thermal divergence in the mantle beginning 2.5 ga: geochemical constraints from greenstone basalts and komatiites. Geoscience Frontiers 7, 543–553.

Condie, K.C., Puetz, S.J., Davaille, A., 2018. Episodic crustal production before 2.7 ga. Precambrian Research 312, 16–22.

Cox, K.G., 1980. A Model for Flood Basalt Vulcanism. Journal of Petrology 21, 629–650. URL: `http://dx.doi.org/10.1093/petrology/21.4.629`.

Crisp, J.A., 1984. Rates of magma emplacement and volcanic output. Journal of Volcanology and Geothermal Research 20, 177–211.

Cutts, K.A., Stevens, G., Hoffmann, J.E., Buick, I.S., Frei, D., Münker, C., 2014. Paleo-to mesoarchean polymetamorphism in the barberton granite-greenstone belt, south africa: Constraints from u-pb monazite and lu-hf garnet geochronology on the tectonic processes that shaped the belt. Bulletin 126, 251–270.

Davies, G.F., 1995. Punctuated tectonic evolution of the Earth. Earth and Planetary Science Letters 136, 363–379.

Dhuime, B., Hawkesworth, C.J., Cawood, P.A., Storey, C.D., 2012. A change in the geodynamics of continental growth 3 billion years ago. Science 335, 1334–1336.

Elkins-Tanton, L.T., 2007. Continental magmatism, volatile recycling, and a heterogeneous mantle caused by lithospheric gravitational instabilities. Journal of Geophysical Research: Solid Earth 112.

Fischer, R., Gerya, T., 2016a. Early earth plume-lid tectonics: A high-resolution 3d numerical modelling approach. Journal of Geodynamics 100, 198–214.

Fischer, R., Gerya, T., 2016b. Regimes of subduction and lithospheric dynamics in the precambrian: 3d thermomechanical modelling. Gondwana Research 37, 53–70.

Ganne, J., Feng, X., 2017. Primary magmas and mantle temperatures through time. Geochemistry, Geophysics, Geosystems 18, 872–888. URL: `https://doi.org/10.1002/2016GC006787`, doi:10.1002/2016GC006787.

Gerya, T., Perchuk, L., Burg, J.P., 2008. Transient hot channels: perpetrating and regurgitating ultrahigh-pressure, high-temperature crust–mantle associations in collision belts. Lithos 103, 236–256.

Gerya, T.V., 2014. Precambrian geodynamics: concepts and models. Gondwana Research 25, 442–463.

Gerya, T.V., Meilick, F.I., 2011. Geodynamic regimes of subduction under an active margin: effects of rheological weakening by fluids and melts. Journal of Metamorphic Geology 29, 7–31. URL: `http://doi.wiley.com/10.1111/j.1525-1314.2010.00904.x`, doi:10.1111/j.1525-1314.2010.00904.x.

Green, E.C.R., White, R.W., Diener, J.F.A., Powell, R., Holland, T.J.B., Palin, R.M., 2016. Activity–composition relations for the calculation of partial melting equilibria in metabasic rocks. Journal of Metamorphic Geology 34, 845–869.

Hamilton, W.B., 2007. Earth's first two billion years—the era of internally mobile crust. Geological Society of America Memoirs 200, 233–296.

Herzberg, C.T., Condie, K.C., Korenaga, J., 2010. Thermal history of the Earth and its petrological expression. Earth and Planetary Science Letters 292, 79–88. URL: `http://dx.doi.org/10.1016/j.epsl.2010.01.022`, doi:10.1016/j.epsl.2010.01.022.

Hickman, A.H., Van Kranendonk, M.J., 2012. Early Earth evolution: evidence from the 3.5-1.8 Ga geological history of the Pilbara region of Western Australia. Episodes 35, 283–297.

Hirth, G., Kohlstedt, D., 2004. Rheology of the upper mantle and the mantle wedge: A view from the experimentalists. Inside the subduction Factory 138, 83–105.

Holland, T.J.B., Powell, R., 2003. Activity–composition relations for phases in petrological calculations: an asymmetric multicomponent formulation. Contributions to Mineralogy and Petrology 145, 492–501.

Holland, T.J.B., Powell, R., 2011. An improved and extended internally consistent thermodynamic dataset for phases of petrological interest, involving a new equation of state for solids. Journal of Metamorphic Geology 29, 333–383.

van Hunen, J., van den Berg, A.P., 2008. Plate tectonics on the early earth: limitations imposed by strength and buoyancy of subducted lithosphere. Lithos 103, 217–235.

Jagoutz, O., 2014. Arc crustal differentiation mechanisms. Earth and Planetary Science Letters 396, 267–277.

Jagoutz, O., Kelemen, P.B., 2015. Role of arc processes in the formation of continental crust. Annual Review of Earth and Planetary Sciences 43, 363–404.

Jahn, B.M., Glikson, A.Y., Peucat, J.J., Hickman, A.H., 1981. Ree geochemistry and isotopic data of archean silicic volcanics and granitoids from the pilbara block, western australia: implications for the early crustal evolution. Geochimica et Cosmochimica Acta 45, 1633–1652.

Johnson, T.E., Brown, M., Gardiner, N.J., Kirkland, C.L., Smithies, R.H., 2017. Earth's first stable continents did not form by subduction. Nature 543, 239–242.

Johnson, T.E., Brown, M., Kaus, B.J.P., VanTongeren, J.A., 2013. Delamination and recycling of Archaean crust caused by gravitational instabilities. Nature Geoscience 7, 47–52. URL: `http://www.nature.com/doifinder/10.1038/ngeo2019`, doi:10.1038/ngeo2019.

Kamber, B.S., 2015. The evolving nature of terrestrial crust from the hadean, through the archaean, into the proterozoic. Precambrian Research 258, 48–82.

Kaus, B.J., 2010. Factors that control the angle of shear bands in geodynamic numerical models of brittle deformation. Tectonophysics 484, 36–47.

Kaus, B.J.P., Mühlhaus, H., May, D.A., 2010. A stabilization algorithm for geodynamic numerical simulations with a free surface. Physics of the Earth and Planetary Interiors 181, 12–20. URL: `http://linkinghub.elsevier.com/retrieve/pii/S0031920110000877`, doi:10.1016/j.pepi.2010.04.007.

Kranendonk, M.J.V., Hickman, A.H., Smithies, R.H., Nelson, D.R., Pike, G., 2002. Geology and tectonic evolution of the archean north pilbara terrain, pilbara craton, western australia. Economic Geology 97, 695–732.

Kump, L.R., Barley, M.E., 2007. Increased subaerial volcanism and the rise of atmospheric oxygen 2.5 billion years ago. Nature 448, 1033–1036. URL: `http://dx.doi.org/10.1038/nature06058` `http://www.nature.com/nature/journal/v448/n7157/suppinfo/nature06058_S1.html`.

Lourenço, D.L., Rozel, A.B., Gerya, T., Tackley, P.J., 2018. Efficient cooling of rocky planets by intrusive magmatism. Nature Geoscience 11, 322.

Martin, H., Moyen, J.F., Guitreau, M., Blichert-Toft, J., Le Pennec, J. L, 2014. Why Archaean TTG cannot be generated by MORB melting in subduction zones. Lithos 198-199, 1–13. URL: `http://dx.doi.org/10.1016/j.lithos.2014.02.017`, doi:10.1016/j.lithos.2014.02.017.

Moore, W.B., Webb, A.A.G., 2013. Heat-pipe earth. Nature 501, 501–505.

Moyen, J.F., 2011. The composite Archaean grey gneisses: Petrological significance, and evidence for a non-unique tectonic setting for Archaean crustal growth. Lithos 123, 21–36. doi:https://doi.org/10.1016/j.lithos.2010.09.015.

Moyen, J.F., Martin, H., 2012. Forty years of TTG research. Lithos 148, 312–336.

Moyen, J.F., Stevens, G., 2006. Experimental constraints on TTG petrogenesis: implications for Archean geodynamics. Archean geodynamics and environments , 149–175.

Moyen, J.F., Van Hunen, J., 2012. Short-term episodicity of Archaean plate tectonics. Geology 40, 451–454.

O'Neill, C., Lenardic, A., Condie, K.C., 2015. Earth's punctuated tectonic evolution: cause and effect. Geological Society, London, Special Publications 389, 17–40.

Palin, R.M., White, R.W., Green, E.C., 2016a. Partial melting of metabasic rocks and the generation of tonalitic–trondhjemitic–granodioritic (ttg) crust in the archaean: Constraints from phase equilibrium modelling. Precambrian Research 287, 73–90.

Palin, R.M., White, R.W., Green, E.C., Diener, J.F., Powell, R., Holland, T.J., 2016b. High-grade metamorphism and partial melting of basic and intermediate rocks. Journal of Metamorphic Geology 34, 871–892.

Powell, R., Holland, T., 1988. An internally consistent dataset with uncertainties and correlations: 3. applications to geobarometry, worked examples and a computer program. Journal of metamorphic Geology 6, 173–204.

Ranalli, G., 1995. Rheology of the earth, 413 pp.

Rapp, R.P., Shimizu, N., Norman, M.D., 2003. Growth of early continental crust by partial melting of eclogite. Nature 425, 605–609. URL: `http://dx.doi.org/10.1038/nature02031` `http://10.0.4.14/nature02031`.

Riel, N., Bouilhol, P., van Hunen, J., Cornet, J., Magni, V., Grigorova, V., Velic, M., 2018. Interaction between mantle-derived magma and lower arc crust: quantitative reactive melt flow modelling using styx. Geological Society, London, Special Publications 478, SP478–6.

Rozel, A.B., Golabek, G.J., Jain, C., Tackley, P.J., Gerya, T.V., 2017. Continental crust formation on early Earth controlled by intrusive magmatism. Nature 545, 47–52.

Rubin, A.M., 1993. Dikes vs. diapirs in viscoelastic rock. Earth and Planetary Science Letters 119, 641–659.

Rummel, L., Kaus, B.J., White, R.W., Mertz, D.F., Yang, J., Baumann, T.S., 2018. Coupled petrological-geodynamical modeling of a compositionally heterogeneous mantle plume. Tectonophysics 723, 242–260.

Rushmer, T., 1995. An experimental deformation study of partially molten amphibolite: Application to low-melt fraction segregation. Journal of Geophysical Research: Solid Earth 100, 15681–15695.

Schmidt, M.W., Poli, S., 1998. Experimentally based water budgets for dehydrating slabs and consequences for arc magma generation. Earth and Planetary Science Letters 163, 361–379.

Sizova, E., Gerya, T., Brown, M., 2014. Contrasting styles of phanerozoic and precambrian continental collision. Gondwana Research 25, 522–545.

Sizova, E., Gerya, T.V., Brown, M., Perchuk, L.L., 2010. Subduction styles in the Precambrian: Insight from numerical experiments. Lithos 116, 209–229. URL: `http://dx.doi.org/10.1016/j.lithos.2009.05.028`, doi:10.1016/j.lithos.2009.05.028.

Sizova, E., Gerya, T.V., Stüwe, K., Brown, M., 2015. Generation of felsic crust in the Archean: A geodynamic modeling perspective. Precambrian Research 271, 198–224. URL: `http://dx.doi.org/10.1016/j.precamres.2015.10.005`, doi:10.1016/j.precamres.2015.10.005.

Sleep, N.H., 2000. Evolution of the mode of convection within terrestrial planets. Journal of Geophysical Research: Planets 105, 17563–17578.

Thielmann, M., Kaus, B.J., 2012. Shear heating induced lithospheric-scale localization: Does it result in subduction? Earth and Planetary Science Letters 359, 1–13.

Van Hunen, J., Moyen, J.F., 2012. Archean subduction: fact or fiction? Annual Review of Earth and Planetary Sciences 40, 195–219.

Van Kranendonk, M.J., 2010. Two types of Archean continental crust: Plume and plate tectonics on early Earth. American Journal of Science 310, 1187–1209.

Van Kranendonk, M.J., Hugh Smithies, R., Hickman, A.H., Champion, D., 2007. secular tectonic evolution of archean continental crust: interplay between horizontal and vertical processes in the formation of the pilbara craton, australia. Terra Nova 19, 1–38.

White, R., Powell, R., Clarke, G.L., 2002. The interpretation of reaction textures in Fe-rich metapelitic granulites of the Musgrave Block, central Australia: constraints from mineral equilibria calculations in the system K_2O-FeO-MgO-Al_2O_3-SiO_2-H_2O-TiO_2-Fe_2O_3. Journal of metamorphic Geology 20, 41–55.

White, R.W., Powell, R., Holland, T.J.B., Johnson, T.E., Green, E.C.R., 2014. New mineral activity–composition relations for thermodynamic calculations in metapelitic systems. Journal of Metamorphic Geology 32, 261–286.

White, R.W., Powell, R., Holland, T.J.B., Worley, B.A., 2000. The effect of TiO_2 and Fe_2O_3 on metapelitic assemblages at greenschist and amphibolite facies conditions: mineral equilibria calculations in the system K_2O-FeO-MgO-Al_2O_3-SiO_2-H_2O-TiO_2-Fe_2O_3. Journal of Metamorphic Geology 18, 497–512.

White, S.M., Crisp, J.A., Spera, F.J., 2006. Long-term volumetric eruption rates and magma budgets. Geochemistry, Geophysics, Geosystems 7.

Wiemer, D., Schrank, C.E., Murphy, D.T., Wenham, L., Allen, C.M., 2018. Earth's oldest stable crust in the pilbara craton formed by cyclic gravitational overturns. Nature Geoscience 11, 357.

Wyman, D., 2013. A critical assessment of neoarchean "plume only" geodynamics: evidence from the superior province. Precambrian Research 229, 3–19.

Zegers, T.E., van Keken, P.E., 2001. Middle Archean continent formation by crustal delamination. Geology 29, 1083–1086.

Table A1: Reference Test (S1T1a1) input data. All the rock types have the same friction angle ϕ_{dry}=30°, same cohesion, $C = 20MPa$ and same shear modulus, $G = 5 * 10^{10}$ Pa. The activaction volume for all the rocks types except for the dislocation creep of Dry olivine is V$_{act}$= 5*10^{-6} m^{3}mol^{-1}, meanwhile for the latter is V$_{act}$= 1.5 m^{3}mol^{-1}. Diffusion creep: p=3.0 while d = 10 m^{-3}. The thermal expansivity is α=3*10^{-5} °Cm^{-1}. The compressibility is equal to β= 0.3 * 10^{-11} Pa^{-1} (valid only for the felsic crust density law). C$_p$ =1050 $J/K/Kg$ for all the rock types.Heat conductivity (see (Clauser and Huenges, 1995; **?**)). **Rheology flow law** (a):(Hirth and Kohlstedt, 2004);(b):(Ranalli, 1995).**Phase Diagram** (1):(Johnson et al., 2013);(2):(Palin et al., 2016a) .**Heat conductivity**:A:k$_1$=0.64,k$_2$=1293, k$_3$=4;B:k$_1$=1.18,k$_2$=474, k$_3$=4;C:k$_1$=0.64,k$_2$=807, k$_3$=4(Clauser and Huenges, 1995; **?**); **Melt extraction data**: [1] I$_R$ (intrusion/extrusion)=50%;M1=0.5%;M2=0.2%;M3=25%. Mantle dep 2 does not produce any melt;[2]:M1=3%;M2=0.0%;M3=25%,I$_R$=100%; Intrusion and Basaltic stage 4 does not produce any melt.[2*] M3 = 20%. All the changes done are listed in Table S2

Phase Name	Flow Law	A_D Pa$^{-n}s^{-1}$	E$_{act}$ Jmol^{-1}	n	Q_l Jkg^{-1}	K Wm^{-1}K^{-1}	H_r $\mu W m^{-3}$	Phase Diagram
Astenophere[1]	Dry Olivile Dsl(a)	1.1*10^{-16}	530*10^3	3.5	380*10^3	A	0.066	Fertile Mantle(1)
Lithospheric M. [1]							0.044	Mantle Depleted (1)
Mantle D.Step 1[1]	Dry Olivile Diff(a)	1.1*10^{-16}	375*10^3	0			0.044	Mantle Dep.(1)
Mantle D.Step 2[1]					//		0.022	Mantle Dep. w.m.(1)
Basalt Step 1[2]	W.Quartzite Disl(b)	5.07*10^{-18}	154*10^3	2.3	380*10^3	B	0.88	EAT B1 (2)
Basalt Step 2[2]							0.69	EAT B2 (2)
Basalt Step 3[2]							0.5	EAT B3 (2)
Basalt Type 2[2]							0.88	EAT B1 (2)
Basalt Step 4[2]	Maf. Granulite Disl(a)	8.83*10^{-22}	445*10^3	4.2	//	B	0.25	EAT B3 (2)
Intrusions [2]							0.25	EAT B3 (2)
Felsic	W.Quartzite Disl(b)	5.07*10^{-18}	154*10^3	2.3	//	C	1.2	Density Law

Table A2: Simulations performed. The relevant input data are listed, all the experiments are based on the reference test, which input data are described in Table.S1. F_0 and F_{fin} are respectively the amount of average felsic crust produced before the drip stage and at the end. C_0 and t_0 are the amount of converted basalts before the drip stage and the timing at which it starts. δt and δT_P are the duration of the drip stage and the mantle potential temperature drop associated with it. $VFel_0$ and $VFel_{fin}$ are the absolute volume of Felsic crust produced before and at the end of the drip stage, and I and R are the relative amount of mafic intrusion and residuum in respect to all the composition field before the drip stage (Ar is the increase of viscosity associated with depletion. Each time the mantle changes composition-e.g. Fertile mantle to mantle depletion stage 1-, the viscosity is increased of a factor 10 or 100; Rh: is the starting rheology, D-D mean dry to dry, W-D wet to dry)

TestName	T_{Moho} °C	ϕ_{dry}	λ_{melt}	F_0	F_{Fin}	C_0	t_0 Myrs	Δt Myrs	ΔT_p °C	$VFel_0$ $km^3 km^{-1}$	$VFel_{fin}$ $km^3 km^{-1}$	I	R
S1T1a1	800	30	0,01	3,6	12,4	19,7	14,3	8,1	125,5	1353,2	7055,0	35,1	11,9
S1T1a2	800	30	0,1	3,6	12,5	19,7	14,3	7,3	124,2	1357,6	7094,4	35,1	11,9
S1T1a3	800	30	0,5	3,6	16,4	19,7	14,3	11,3	112,7	1358,6	9105,4	35,1	11,9
S1T1a4	800	30	1	3,6	13,8	19,7	14,3	5,5	110,3	1358,6	7796,3	35,1	11,9
S1T1b1	1000	30	0,01	2,9	14,3	16,3	4,3	9,6	105,4	1004,2	8322,8	34,6	10,1
S1T1b2	1000	30	0,1	2,9	14,6	16,3	4,3	8,3	103,5	994,0	8829,9	34,6	10,1
S1T1b3	1000	30	0,5	2,9	14,3	16,3	4,3	9,3	100,5	994,0	8248,1	34,6	10,1
S1T1b4	1000	30	1	2,9	14,6	16,3	4,3	9,7	98,0	994,0	8332,5	34,6	10,1
S1T1c1	1200	30	0,01	3,7	14,5	29,6	3,2	7,3	93,7	1257,0	7913,2	33,9	18,3
S1T1c2	1200	30	0,1	3,7	16,1	29,6	3,2	7,6	92,2	1257,7	8802,0	34,0	18,3
S1T1c3	1200	30	0,5	3,7	14,7	29,6	3,2	5,7	93,3	1257,7	8564,3	34,0	18,3
S1T1c4	1200	30	1	3,7	13,7	29,6	3,2	5,7	87,7	1257,8	7530,0	34,0	18,3
S1T1a115	800	15	0,01	4,0	12,1	20,4	14,3	9,6	120,6	1529,6	5890,5	32,3	12,8
S1T1a215	800	15	0,1	3,9	15,6	20,1	14,3	14,2	110,8	1475,8	8451,9	32,3	12,7
S1T1a315	800	15	0,5	3,9	15,2	20,1	14,3	13,9	101,3	1476,3	8748,7	32,3	12,7
S1T1a415	800	15	1	3,9	16,1	20,1	14,3	13,8	98,4	1476,3	9256,6	32,3	12,7
S1T1b115	1000	15	0,01	3,9	18,2	17,9	4,3	15,1	87,5	1331,1	10048,4	31,7	11,4
S1T1b215	1000	15	0,1	3,9	16,4	17,9	4,3	14,9	83,6	1331,1	9308,3	31,7	11,4
S1T1b315	1000	15	0,5	3,9	19,1	17,9	4,3	13,9	82,3	1331,1	10745,8	31,7	11,4
S1T1b415	1000	15	1	3,9	18,2	17,9	4,3	14,5	81,2	1331,1	10312,6	31,7	11,4
S1T1c115	1200	15	0,01	3,5	17,5	32,8	3,3	10,4	71,4	1206,9	9239,8	31,2	21,2
S1T1c215	1200	15	0,1	3,5	15,5	32,8	3,3	11,0	70,8	1207,6	8273,6	31,2	21,3
S1T1c315	1200	15	0,5	3,5	18,4	32,8	3,3	10,6	71,7	1212,9	10031,8	31,2	21,3
S1T1c415	1200	15	1	3,5	17,5	32,8	3,3	11,1	71,2	1213,2	9659,8	31,2	21,3
S1T1a105	800	5	0,01	4,0	14,0	20,5	14,3	14,4	147,1	1533,9	6112,4	32,2	12,9
S1T1a205	800	5	0,1	3,7	9,9	19,4	14,3	7,2	158,8	1396,2	4246,8	35,0	11,7
S1T1a305	800	5	0,5	3,8	12,1	19,4	14,3	10,6	148,5	1422,3	5963,2	35,0	11,7
S1T1b105	1000	5	0,01	2,9	13,9	16,2	4,3	9,4	124,2	995,6	7652,2	34,7	10,1
S1T1b205	1000	5	0,1	2,9	15,3	16,3	4,3	9,7	110,4	997,6	8860,3	34,6	10,1
S1T1b305	1000	5	0,5	2,9	13,4	16,3	4,3	9,0	106,2	994,9	7963,6	34,7	10,1
S1T1b405	1000	5	1	2,9	13,6	16,3	4,3	9,8	99,6	994,9	7883,4	34,7	10,1
S1T1c105	1200	5	0,01	3,7	15,2	29,6	3,2	8,1	101,4	1258,6	8754,7	33,9	18,4
S1T1c205	1200	5	0,1	3,7	13,5	29,6	3,2	8,6	97,7	1256,6	7530,6	33,9	18,4
S1T1c305	1200	5	0,5	3,7	14,8	29,6	3,2	8,1	95,1	1258,7	8324,9	33,9	18,3
S1T1c405	1200	5	1	3,7	13,8	29,6	3,2	6,6	96,6	1258,8	8003,0	33,9	18,3
	A_r	Rh	T_{Moho} °C										
S2T1A1DD	10	DD	800	3,6	12,4	20,1	14,3	10,7	135,9	1366,1	7007,7	35,2	12,1
S2T1A1DDb	10	DD	1000	4,7	14,9	22,5	9,3	4,7	105,7	1704,1	9049,3	35,1	13,4
S2T1A1DDc	10	DD	1200	3,3	13,3	30,9	4,3	5,7	96,2	1156,2	8247,0	34,1	19,3
S2T1A2DD	100	DD	800	5,6	11,0	25,6	19,3	5,8	129,6	2213,9	6377,3	35,4	14,8
S2T1A2DDb	100	DD	1000	4,8	12,7	22,6	9,3	5,8	98,1	1741,2	7484,0	35,0	13,5
S2T1A2DDc	100	DD	1200	3,4	12,4	30,8	4,3	7,1	86,0	1189,2	7601,2	34,2	19,1
S2T1A0WD	1	WD	800	3,5	11,9	15,1	9,3	8,7	138,0	1370,4	6796,6	34,3	9,3
S2T1A1WD	10	WD	800	5,1	10,6	18,1	14,3	3,3	139,7	2036,3	5991,5	34,5	10,7
	I_R	M2											
S3T1M0020	20	0,2		5,3	14,9	21,1	14,3	11,6	132,5	2024,8	10345,0	30,3	13,4
S3T1M0035	35	0,2		4,0	13,9	16,7	14,3	8,0	122,6	1504,8	9396,0	31,9	10,6
S3T1M0065	65	0,2		3,7	13,7	19,3	14,2	8,0	130,8	1398,3	5833,0	38,7	10,9
S3T1M0080	80	0,2		1,4	8,2	13,6	9,3	15,0	140,3	498,6	2081,3	42,4	7,7
S3T1M1050	50	2		2,0	12,4	11,4	0,8	9,5	115,2	701,2	7000,1	32,5	7,5
S3T1M1065	65	2		1,5	10,6	9,9	0,8	5,9	110,8	552,5	4776,3	36,4	6,2
S3T1M1080	80	2		1,3	9,4	9,5	0,8	4,0	114,7	451,9	3209,7	40,4	5,6
	T_P °C	Thikckness km	M2										
S4T180A	1450	80	0,2	12,4	18,3	72,8	64,3	4,9	75,7	3655,3	8167,2	34,8	38,3
S4T180B	1500	80	0,2	7,7	15,6	38,6	29,3	7,9	109,1	2552,6	7571,4	33,0	22,7
S4T180D	1600	80	0,2	3,2	12,5	15,8	7,5	8,8	188,9	1427,9	6387,9	34,9	9,7
S4T180A_{m2}	1450	80	2	8,3	15,3	51,4	42,6	5,1	76,1	2384,9	6678,5	35,1	28,9
S4T180B_{m2}	1500	80	2	5,7	16,3	28,6	18,8	6,5	89,3	1859,4	7881,4	33,0	17,5
S4T180D_{m2}	1600	80	2	2,4	11,2	9,0	0,6	9,9	157,2	1036,8	6721,9	33,9	5,6
S4T1100A	1450	100	0,2	14,0	15,7	82,2	74,2	4,9	82,6	4472,7	7052,7	36,0	41,1
S4T1100B	1500	100	0,2	7,8	16,2	46,7	44,3	10,1	103,0	2737,8	7064,5	35,5	26,4
S4T1100C	1550	100	0,2	5,3	14,6	26,5	24,3	9,1	136,7	2116,7	7946,2	33,4	16,0
S4T1100D	1600	100	0,2	2,8	12,3	14,9	9,2	11,2	178,2	1219,2	6889,7	34,4	9,2
S4T1120A	1450	120	0,2	9,5	18,4	58,8	59,3	7,2	90,3	3468,1	8011,1	35,8	32,1
S4T1120B	1500	120	0,2	9,1	17,5	58,0	59,3	8,0	113,3	3434,1	8453,7	36,7	31,4
S4T1120C	1550	120	0,2	6,2	14,6	40,1	34,3	7,6	155,8	2573,6	8002,1	35,5	23,3
S4T1120D	1600	120	0,2	4,0	11,6	19,3	14,3	9,7	191,1	1812,9	7224,7	34,7	11,7